Remote Sensing of Environment 296 (2023) 113751

Contents lists available at ScienceDirect

Remote Sensing of Environment

journal homepage: www.elsevier.com/locate/rse

Multi-source data analysis to assess the past and present kinematics of the *Pisciotta* Deep-Seated Gravitational Slope Deformation (southern Italy)

Matteo Albano [a], Michele Saroli [b,a,*], Lisa Beccaro [a], Marco Moro [a], Fawzi Doumaz [a], Marco Emanuele Discenza [c], Luca Del Rio [a], Matteo Rompato [b]

[a] Istituto Nazionale di Geofisica e Vulcanologia, via di Vigna Murata 605, 00143 Roma, Italy
[b] Dipartimento di Ingegneria Civile e Meccanica, Università degli Studi di Cassino e del Lazio meridionale, via G. di Biasio 43, 03043 Cassino, FR, Italy
[c] Geoservizi s.r.l., Via Luigi e Nicola Marinelli 2, 86025 Ripalimosani, CB, Italy

ARTICLE INFO

Edited by Jing M. Chen

Keywords:
DSGSD
Drone survey
InSAR
Optical data
Numerical modeling

ABSTRACT

Although Deep-Seated Gravitational Slope Deformations are well-known in the literature, their evolution and kinematics are still poorly understood. Their behavior is often complex and characterized by small movements associated with steady-state creep, alternating with periods of stasis, or accelerating downslope movements that, in some cases, could result in sudden and catastrophic failure events. Therefore, a multidisciplinary approach is often required. In this work, we shed light on the complex geometry and kinematics of the *Pisciotta* DSGSD, a deep-seated roto-translational sliding involving structurally complex turbiditic rock mass and interacting with man-made infrastructures. To reveal the geometrical features and the spatial and temporal behavior of the analyzed phenomenon, a multidisciplinary investigation was performed. Typical DSGSD landforms were mapped employing in-situ surveys, aided by stereoscopic analysis of historical aerial images and high-resolution drone-based mapping. Structural data and ancillary ground-based surveys revealed the presence of a highly weathered and folded turbiditic sequence, with competent sandstone and calcarenite units alternated by tectonically disrupted, weak argillite and mudrock layers. Remote sensing measurements from optical imagery and Synthetic Aperture Radar satellite data assessed the DSGSD's past and current kinematics, allowing to distinguish a pre-failure period with accelerating displacement rates, a failure period with maximum displacement rates, and a current post-failure period with decelerating displacement rates. Analytical modeling established the deep reach (up to 85 m) of the studied DSGSD as it allowed the estimation of its bottom surface and volume, as verified by available boreholes and inclinometric measurements. Furthermore, numerical modeling outcomes highlighted how the progressive weakening and alteration of the DSGSD material, in conjunction with changes in groundwater dynamics, serve as the primary mechanisms driving the observed kinematics. The models also revealed the intricate interaction between the DSGSD and the neighboring infrastructures.

1. Introduction

Deep-Seated Gravitational Slope Deformations (DSGSDs) include a group of complex slope movements, commonly affecting high-relief or steep mountain slopes and characterized by low displacement rates over long time intervals (Agliardi et al., 2012; Discenza and Esposito, 2021). These phenomena occur in many lithological, geomorphological, and structural conditions (Pánek and Klimeš, 2016), and typically manifest on landscapes with downhill- or uphill-facing scarps, shifted ridge lines, multi-crested ridges, tension cracks, grabens, enclosed depressions, rotated blocks, slope bulges, narrowing of valley floors, and secondary, nested landslides (Agliardi et al., 2012; Ambrosi and Crosta, 2011; Crosta et al., 2013; Discenza and Esposito, 2021; Pánek and Klimeš, 2016). Several factors control the spatial and temporal evolution of such instabilities: topography and slope geometry (Ambrosi and Crosta, 2011; Crosta et al., 2013), lithological and geological setting (Chalupa et al., 2021; Jaboyedoff, 2011), debuttressing (Jaboyedoff, 2011), glacial rebound (Crosta et al., 2013; Jarman and Harrison, 2019), changes in slope groundwater regime (Agliardi et al., 2020; Notti et al., 2021), climate fluctuations (Livio et al., 2022), gravitational and

* Corresponding author at: Dipartimento di Ingegneria Civile e Meccanica, Università degli Studi di Cassino e del Lazio meridionale, via G. di Biasio 43, 03043 Cassino, FR, Italy.
E-mail address: michele.saroli@unicas.it (M. Saroli).

https://doi.org/10.1016/j.rse.2023.113751
Received 17 February 2023; Received in revised form 5 July 2023; Accepted 5 August 2023
Available online 12 August 2023

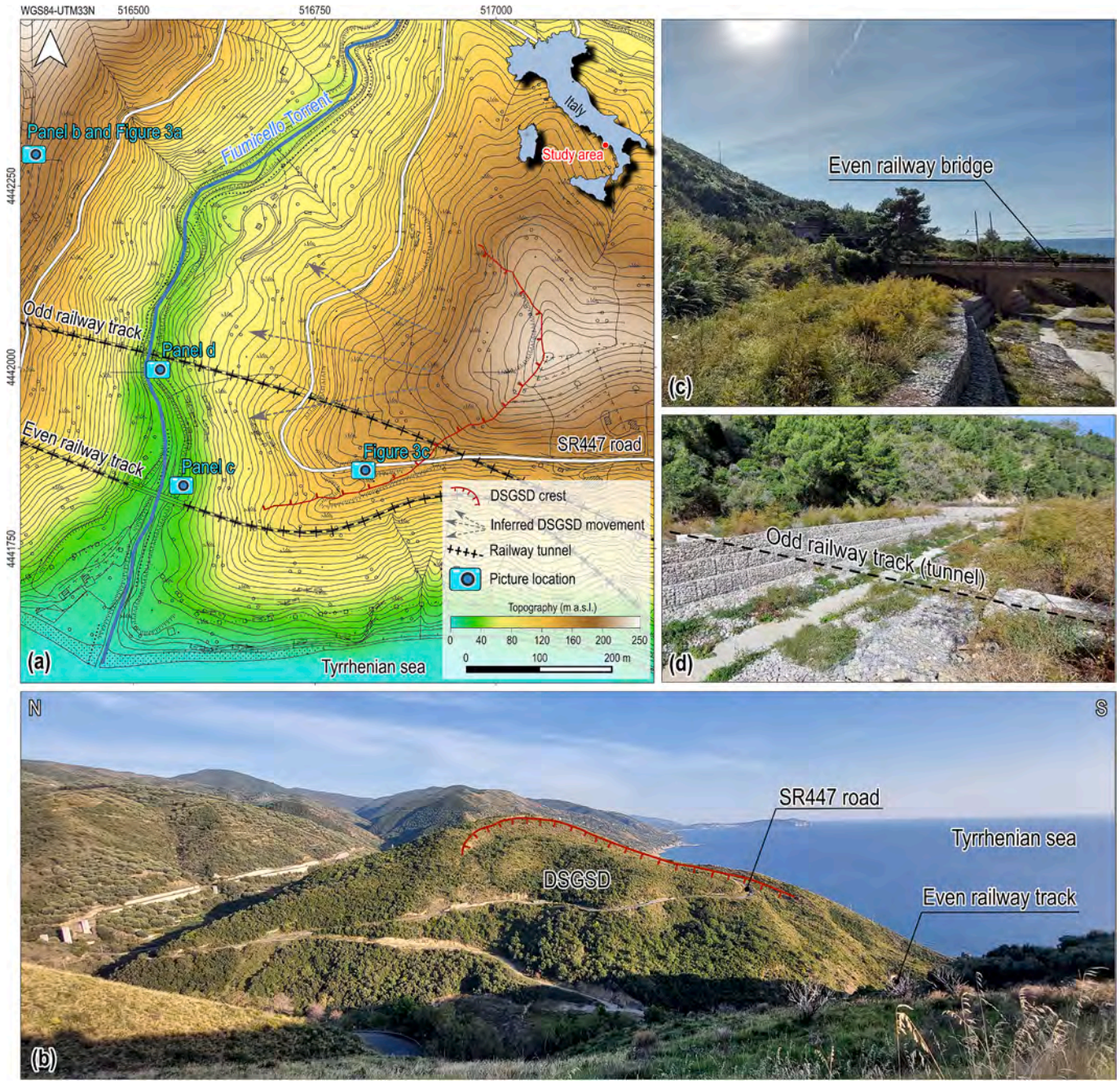

Fig. 1. Overview of the study area. (a) Current setting and location of the DSGSD area with the indication of the DSGSD crest, its inferred movement, the main interfering infrastructures, and the location of pictures in panels b, c and d. (b) Panoramic view of the DSGSD area with the indication of the main DSGSD crest (the red line). (c) Even railway bridge crossing the *Fiumicello* Torrent. (d) Current setting of the odd railway artificial tunnel crossing of the *Fiumicello* Torrent. For the location of the pictures, see panel a. (For interpretation of the references to colour in this figure legend, the reader is referred to the web version of this article.)

tectonic stress changes (Esposito et al., 2021), karst, dissolution, rock/soil weakening (Discenza et al., 2020, 2011), and seismicity (Moro et al., 2011; Saroli et al., 2021). Their kinematics is often complex and characterized by small movements associated with steady-state creep, alternating with periods of stasis or accelerating downslope movements that, in some cases, could result in sudden and catastrophic failure events (Barla and Paronuzzi, 2013; Chigira et al., 2013; Pedrazzini et al., 2013). Even though DSGSD rarely claim lives, they can cause severe damage to buildings and infrastructures (Lacroix et al., 2020; Mansour et al., 2011). Therefore, a comprehensive understanding of DSGSDs dynamics is required to identify appropriate measures that mitigate risks, safeguard infrastructures, and ensure the safety of affected areas.

Investigating DSGSDs poses significant challenges for researchers due to their intricate nature and prolonged evolution. A comprehensive understanding of their complex behavior requires meticulous data collection, thorough analysis, and careful interpretation across various scales (Crosta et al., 2014). These slow-moving processes unfold over decades to millennia, demanding extensive long-term datasets and the identification of key factors that influence their development over extended periods (Discenza et al., 2011; Pánek and Klimeš, 2016).

Acquiring accurate and high-quality data is challenging. Indeed, installing and maintaining in-situ monitoring systems can be costly and time-consuming (Yamamoto et al., 2023), while remote sensing techniques may have limitations in capturing small-scale deformations or

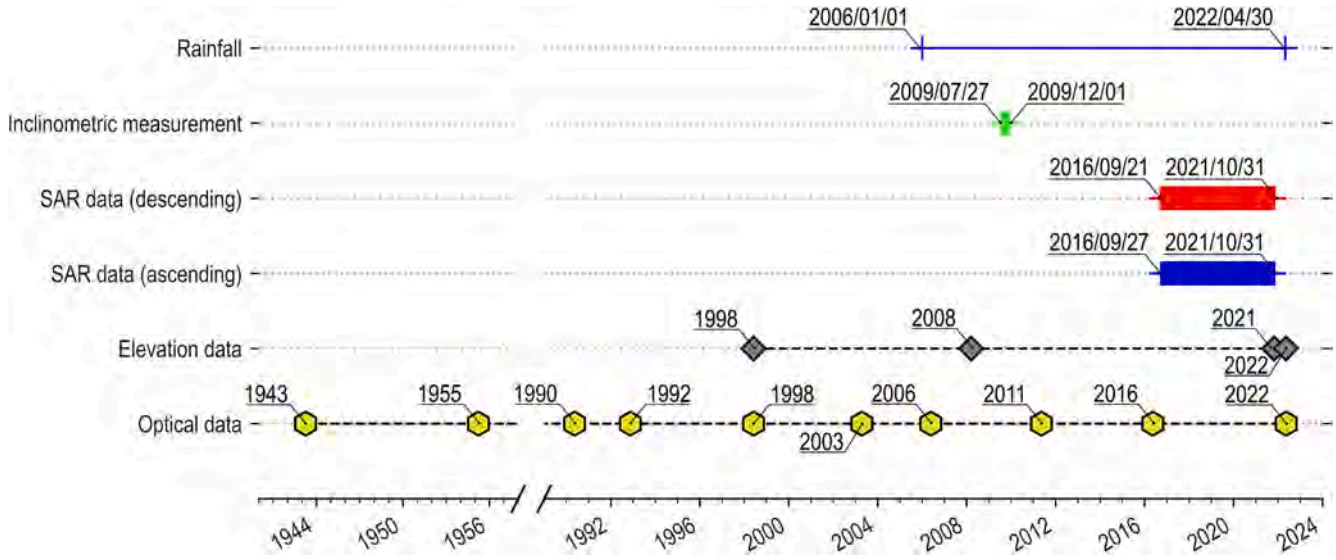

Fig. 2. Time coverage of the ground-based and remote sensing datasets acquired over the study area.

require frequent revisits for precise temporal changes. Integrating diverse data sources, including field measurements, remote sensing data, and geological/geotechnical information, also requires robust methods to extract meaningful insights and comprehend the complex interactions within DSGSDs (Casagli et al., 2023; Crosta et al., 2014; Jaboyedoff, 2011; Notti et al., 2021). Moreover, uncertainties in input data, coupled with the complex interplay of various factors and limited understanding of triggering mechanisms, make predicting DSGSD behavior and assessing associated hazards a daunting task.

In this study, we adopted a multidisciplinary approach to examine the kinematics of the *Pisciotta* DSGSD, which serves as a significant example of a slow-moving gravitational-induced deformation. By integrating various data sources, such as field measurements, remote sensing data, and geological/geotechnical information, we were able to unveil for the first time the kinematics of the DSGSD from its initial stages to its current state. Moreover, through analytical and numerical analyses, we gained further insights into the DSGSD's geometry, the factors influencing its evolution and kinematics, and its relationship with nearby infrastructures. This comprehensive investigation has shed light on the intricate dynamics of the *Pisciotta* DSGSD, providing valuable knowledge for future research and mitigation efforts.

1.1. The case study

Known since 1960, the *Pisciotta* DSGSD is located near the coast of the Tyrrhenian Sea (lat: 40.128320°; lon: 15.196330°) in the south of Italy (Fig. 1a and b). It fully develops within an open-basin, deep-water, calcareous-siliciclastic turbiditic sequence, known in the literature as the *Saraceno* Formation (Bonardi et al., 2009; Ciarcia et al., 2012; De Blasio et al., 1978; Vezzani, 1968). The unit, several hundred meters thick, is composed of medium-fine sandstones and carbonate-arenites in medium-to-thick beds, alternated with foliated argillites (Martelli et al., 2016).

Regarding the climate of the study area, it can be described as Mediterranean, featuring mild winters and hot summers. Snowfall is infrequent, while rainfall occurs more regularly, occasionally accompanied by extreme weather events. Historical, instrumental, and seismological data categorize this region as a moderate to low seismic risk. An analysis of the Italian Macroseismic database (Locati et al., 2022) revealed the occurrence of twelve earthquakes, with magnitudes ranging from 4 to 6.8, which resulted in macroseismic intensities ranging from 2 (scarcely felt) to 6 (slightly damaging) in the nearby municipality of *Pisciotta* (refer to supplementary Fig. S1a and b). The estimated peak ground acceleration (PGA) at the bedrock for the study area ranges between 0.075 and 0.1 g for a 10% probability of exceedance in 50 years (supplementary fig. S1a) (Rovida et al., 2022; Stucchi et al., 2011).

The movement of the *Pisciotta* DSGSD towards the *Fiumicello* riverbed clearly manifested in the 1980s, with average rates of about 1 m per year (De Vita et al., 2013). This movement caused several damages to nearby infrastructures, including the SS447 road and the *Salerno-Reggio Calabria* railway bridges (Fig. 1c and Fig. S2a). The road experienced continuous distortions, cracking, bulging, and tilting of pavement, guardrails, and retaining walls, leading to traffic interruptions. The railway tunnel, crossing the DSGSD at its foot, was affected as well. The sliding mass progressively obstructed the *Fiumicello* riverbed and reduced the freeboard under the odd railway bridge (Fig. S2a). In 2008, a severe flood resulted in the damming of the riverbed at the odd railway bridge, flooding the tunnel and disrupting rail transport on both tracks.

Countermeasures were implemented in the 2018–2020 period, such as replacing the bridge with an artificial tunnel and raising the *Fiumicello* riverbed (Fig. 1d) to mitigate the flooding risk (Italferr S.p.A, 2013a). However, the impact of such an intervention on the slope stability and kinematics has not been quantified. Moreover, limited information is available on the slope-tunnel interaction, with reported small cracks in the tunnel lining and water leaks in the odd railway tunnel (Italferr S.p.A, 2013b).

Several studies investigated the *Pisciotta* DSGSD's kinematics, extent, and temporal behavior using laser scanning, satellite imagery, borehole data, inclinometer monitoring, and geological surveys (Barbarella et al., 2018, 2015; Barbarella and Fiani, 2013; De Vita et al., 2013, 2017). However, a comprehensive quantitative description of the DSGSD's past and current kinematics, the factors influencing its evolution, and its relationship with neighboring infrastructures is still lacking.

2. Data and methods

To bridge this knowledge gap, we undertook an extensive analysis by integrating and analyzing a vast dataset encompassing a time span of approximately 78 years (Fig. 2). This dataset included a diverse range of remote sensing data, such as Synthetic Aperture Radar (SAR), high-resolution satellite and airborne imagery, and drone-based ultra-high-resolution imagery. In addition, we incorporated ground-based measurements, including rainfall data, borehole logs, laboratory tests, inclinometric measurements, and geomorphological surveys. Ancillary information, such as topographic maps at various scales and airborne

Fig. 3. Pictures of the drone survey performed over the *Pisciotta* DSGSD. (a) Panoramic view of the take-off and landing site of the drone and the *Pisciotta* DSGSD. (b) Detail of the drone. (c) Measurement operation of mobile GCPs coordinates with a GPS/RTK receiver. For the location of pictures, see Fig. 1a.

Lidar data, played a crucial role in interpreting the gathered data.

To gain a comprehensive understanding of the *Pisciotta* DSGSD, we employed analytical and numerical approaches. These methods allowed us to estimate the DSGSD's geometry, quantify its past and current behavior, investigate about the possible factors affecting its kinematics, and identify any potential interactions with the surrounding infrastructures. By utilizing this combined analytical and numerical framework, we were able to shed light on the intricate dynamics of the DSGSD and enhance our knowledge of its behavior over time.

2.1. Field campaigns

In the initial stage of the analysis, the geomorphological setting of the slope was reconstructed, based on data acquired during two field campaigns. The first campaign took place on October 26–28, 2021, and the second on May 11–13, 2022. Structural data (n = 134) were collected on the outcrops along the roads crossing the DSGSD body and were geolocated with a handheld GPS (accuracy ±2 m). We systematically measured the attitude of the different structural and stratigraphic elements (i.e., bedding, fractures), which were plotted and analyzed using stereonets (lower hemisphere, Schmidt equal area) within the Stereonet software (Allmendinger et al., 2011). Two drone surveys were also conducted during the two campaigns to acquire a high-resolution orthophoto and a digital surface model (DSM) of the study area. The survey of the DSGSD mass was carried out using a radio-controlled multi-rotor DJI Mavic Pro 2 UAV system, which was equipped with a high-resolution digital camera. This enabled us to capture a series of aerial images of the DSGSD. The take-off and landing area for the drone was situated on the opposite side of the *Fiumicello* Torrent valley (Fig. 3). For more information regarding the drone flights and data processing, please refer to section 1.1 in the supplementary material.

2.2. Remote sensing data and processing

In the second stage, we gathered and analyzed remote sensing data from both optical imagery and SAR, enabling us to map the movements of DSGSD from 1943 to 2022.

2.2.1. Optical imagery

Optical data consist of high-resolution aerial and satellite images acquired between 1943 and 2022 (Fig. 2). Details about the data type and format are reported in section 1.2 in the supplementary material. These data were exploited to investigate the morphological evolution of the DSGSD from 1943 to 2022 following three different approaches.

The first approach consists of a digital stereoscopic analysis on images acquired in stereoscopic mode from 1943 to 2003 to investigate the morphological markers of the DSGSD, such as scarps, counterscarps, trenches, and fissures. We used a Planar SD StereoMirror™ system (https://www.planar.com/support/discontinued-products/stereomirror-displays/) coupled with in-house software that allowed us to align and fuse two stereo-images in a single stereoscopic image (Falcone, 2023). The detected morphological features were vectorized in a GIS

environment. Later, stereoscopic images were orthorectified with the Agisoft Metashape Professional software (Agisoft LLC, 2022) and georeferenced by Ground Control Points (GCPs) in a GIS environment (QGIS Development Team, 2022).

The second approach provided a first estimate of the long-wavelength dynamics of the DSGSD in the period 1943–2022 by tracing the outer boundary of the SR447 road on each available orthorectified image (Fig. 2) and calculating its elongation ratio, given by the following equation:

$$E_r = \frac{l(t_i) - l(t_{i-1})}{t_i - t_{i-1}} \quad (1)$$

where $l(t_i)$ and $l(t_{i-1})$ are the lengths of the road at i and i-1 epochs, respectively.

Finally, the third approach utilized ortho-images captured between 2006 and 2022 to conduct a quantitative kinematic analysis using Digital Image Correlation (DIC) techniques. DIC is a remote sensing technique capable of extracting valuable information regarding ground changes by analyzing images captured at different times but covering the same geographical area. It has proven successful in various domains, including landslides, volcanoes, and earthquakes, and with different data types, such as radar, optical, thermal, and elevation data (Aaron et al., 2021; Bickel and Manconi, 2022; Caporossi et al., 2018; Raack et al., 2020; Storni et al., 2020). For this analysis, we employed an open-source DIC code based on a Fourier transform algorithm (DIC-FFT) (Bickel et al., 2018). The accuracy of the code was estimated to be within 8 to 12% of the observed maximum displacements based on comparisons with GNSS displacements. The code facilitated pre- and post-processing of image pairs by implementing co-registration and filtering techniques.

During the DIC analysis, image pairs were co-registered without image splitting or oversampling using an FFT-based image alignment function implemented in the code (Bickel et al., 2018) to correct for potential rigid shifts between pairs. A window size of 128 × 128 pixels was utilized for the DIC analysis, as it provided an optimal balance between spatial coverage, resolution, processing speed, and correlation quality. The evaluation metric for correlation quality was the root mean square error (RMSE). No oversampling was applied during the correlation process. The x- and y-direction strides (or skips), which determine the shift of the DIC correlation window, were set to $w_i/2$ to ensure accurate representation of the displacement field. Finally, a 6 × 6-pixel median filter was applied to the DIC results to enhance the signal-to-noise ratio.

2.2.2. SAR data

The DSGSD short-wavelength spatial and temporal behavior is further investigated by exploiting level-1 Single Look Complex (SLC) Synthetic Aperture Radar (SAR) data acquired in the Interferometric Wide swath mode by the Sentinel-1 satellite mission. Two long stacks of C-band Sentinel-1A and B data (wavelength $\lambda = 5.547 \times 10^{-2}$ m), acquired along both ascending and descending tracks between September 2016 and October 2021 (Fig. 2), were processed through the Small Baseline Subset (SBAS) multi-temporal method of Differential SAR Interferometry (Berardino et al., 2002; Casu et al., 2006; Lanari et al., 2007) (supplementary Table S1). Analyses were performed with the SARscape software (Sarmap, 2021) operative on the ENVI platform. Considering the geometry of the acquisition system, the predominant movement of the sliding mass, and the mean displacement rates derived from bibliographic information (De Vita et al., 2013), we set the input processing parameters to obtain results with the maximum spatial coverage, the minimum temporal and spatial decorrelation, and the lower uncertainty. A comprehensive description of the processing steps and the adopted parameters can be found in Section 1.3 of the Supplementary material.

2.3. Ancillary data and processing

The interpretation of remote sensing data was enhanced through the integration of various types of ancillary data. These additional datasets included detailed geomorphological and geotechnical surveys, providing information about the landforms and geolithological features of the DSGSD. Furthermore, rainfall data was incorporated to understand the temporal patterns of precipitation, which can significantly influence slope stability and gravitational movements. Additionally, ground elevation data from different sources were integrated, allowing for a comprehensive assessment of the terrain's topography and changes over time.

2.3.1. Geomorphological and geotechnical surveys

Geomorphological investigations and in-situ surveys were commissioned in 2009 by Italferr S.p.A. to assess the DSGSD's characteristics and the geotechnical properties of the involved lithologies (Italferr S.p.A, 2011a, 2011b, 2011c, 2013c). Surveys consisted of seven boreholes cored through the sliding mass at depths up to 110 m. Four boreholes were equipped with vertical inclinometers to identify one or more active sliding surfaces (Fig. 2). The other three boreholes were equipped with open pipe (Norton) and *Casagrande* piezometers to assess the groundwater level. Borehole logs were interpreted in terms of Rock Quality Designation (RQD), defined as the percentage of intact drill core pieces longer than 10 cm recovered during a single core run (Deere and Deere, 1988).

In addition to the borehole data, a variety of undisturbed and reworked samples were collected from different depths to conduct laboratory tests and investigate the physical properties, stiffness, and strength characteristics of the soil and rock (Italferr S.p.A, 2013c). Soil samples underwent laboratory testing to determine their physical and index properties, such as unit weight, water content, Atterberg limits, and grain size distributions. Furthermore, the peak and residual strength of the soil samples were assessed under both drained and undrained conditions. Similarly, rock samples were tested to determine their unit weight and uniaxial compressive strength. The data obtained from these tests were compiled and analyzed to provide a comprehensive geotechnical characterization of both the DSGSD mass and the underlying bedrock. Further details regarding the laboratory test results and the geomechanical characterization can be found in Section 1.4 of the supplementary material.

2.3.2. Rainfall data

Daily rainfall data from January 2006 to April 2022 (Fig. 2) were collected from the Multirisk Centre of the Campania region (http://centrofunzionale.regione.campania.it/#/pages/dashboard) at the *S. Mauro La Bruca* pluviometric station, located at approximately seven kilometers from the study area.

2.3.3. Elevation data

Elevation data were first obtained from the 1:5000 topographic map dated 1998 (Fig. 2), available from the Campania Region Geoportal, to derive a 5x5m grid Digital Terrain Model (DTM) of the area.

Lidar data were collected from the Italian National Geoportal and processed to compute a high-resolution DTM. The point cloud dataset, acquired between February and March 2008 (Fig. 2), is provided in '.laz' format with a point density >1.5 per square meter, a planimetric accuracy (2σ) of 30 cm, and an altimetric accuracy (1σ) of 15 cm.

We processed the point cloud with the LAStools software suite provided by Rapidlasso GmbH company (Isenburg, 2021) and available as a plugin in the QGIS environment (QGIS Development Team, 2022). We exploited the LasGround algorithm to classify the bare-earth points and then calculate the DTM. The main processing parameters such as the step size; the maximal offset up to which points above the current ground estimate get included; the maximal standard deviation for planar patches; and the threshold at which spikes get removed, were set

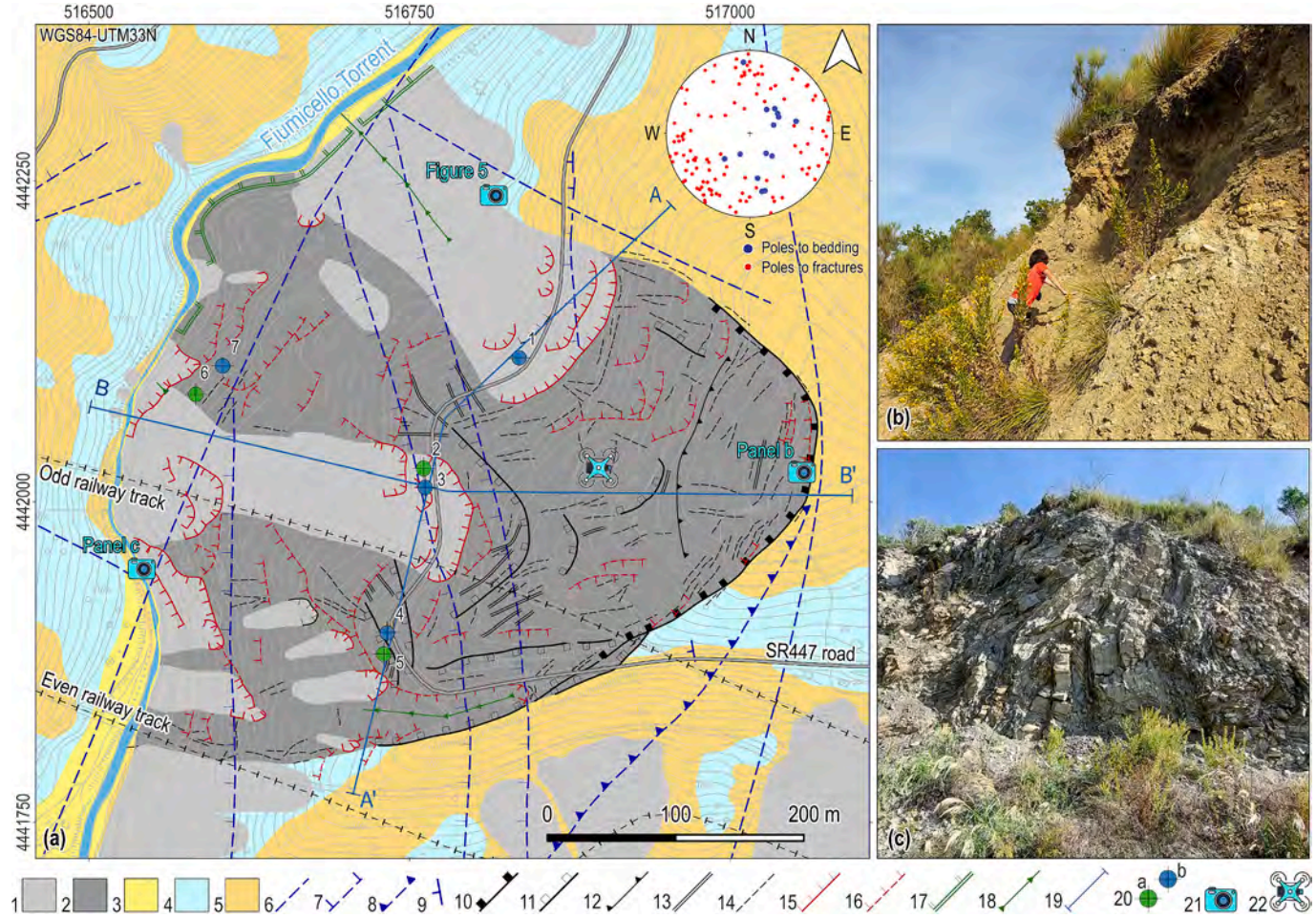

Fig. 4. Geomorphological analysis of the study area. (a) Geomorphological map (modified from Italferr S.p.A (2011a, 2011b, 2011c)). Key to the legend: 1. Shallow landslide deposits; 2. DSGSD; 3. Recent fluvial deposits; 4. Detrital and colluvial deposits; 5. Turbiditic bedrock (sandstones, calcarenites, and argillites); 6. High angle fault; 7. Normal fault; 8. Reverse fault; 9. Bedding; 10. DSGSD main scarp; 11. DSGSD secondary scarp; 12. Uphill-facing scarp; 13. Trench or tension crack; 14. Fissures; 15. Landslide scarp; 16. Morphological scarp; 17. Fluvial scarp; 18. Gully; 19 Trace of the cross-sections in Fig. 6; 20. Boreholes: (a) with piezometer; (b) with inclinometer; 21. Location of pictures in panels b, c, and Fig. 5; 22. Drone flight (supplementary video V1). (b) DSGSD main scarp, consisting of pelitic layers with intercalated 10–30 cm thick arenites. c) Strongly folded and fractured calcarenitic strata interspersed by less competent argillite mudrocks.

according to the optimal values adopted by Barbarella et al. (2019) in the same area.

2.4. Interpretation of the available data

In the third stage, a comprehensive interpretation of all available data was conducted to evaluate the geometric properties of the DSGSD (e.g., its extent and volume), as well as the reconstruction of its kinematics concerning changes in sliding velocity and spatial extent. The analysis also considered specific triggering scenarios such as earthquake loading and changes in groundwater level. By undertaking this analysis, the evolution of the DSGSD was deciphered, leading to the development of a slope evolutionary model. This model not only provided insights into the ongoing changes within the slope but also facilitated an understanding of its interaction with adjacent infrastructures.

2.4.1. DSGSD extent and volume estimation

Once mapped, the displacements obtained from the analysis of optical, elevation, and SAR data were used to determine the spatial extent of the DSGSD. To estimate its volume, various techniques are available (refer to Jaboyedoff et al. (2020) and related references). In our study, we employed the method introduced by Prajapati and Jaboyedoff (2022). This method calculates the bottom surface of the DSGSD and, consequently, its volume by interpolating multiple cubic spline curves. These curves are generated using two endpoints on the boundary of the DSGSD and the first derivative at those points. The method's parameters are defined as the mean dip angles on the left and right sides of the slope line connecting the highest and lowest elevation points along the contour limits of the DSGSD. We selected these parameters to minimize the discrepancy between the predicted depth of the bottom surface and the observed bottom depth from available borehole inclinometers. We utilized the Mean Absolute Error (MAE) as a metric to assess the goodness of fit. Additionally, we validated the resulting surface by comparing it with the sliding surface derived from InSAR ground displacements along a 2D cross-section. This comparison was carried out using the graphical method proposed by Carter and Bentley (1985). For further information on the assumptions and application procedure of the method, please refer to Jaboyedoff et al. (2020).

2.4.2. Slope stability analysis

To enhance our analysis, we created a three-dimensional numerical model specifically designed to simulate a slope that replicates the characteristics (i.e., ground displacement patterns, shear bands evolution) observed in the final stages of evolution, as well as the current conditions of the *Pisciotta* DSGSD. This includes factors such as slope topography, slide boundaries, bottom DSGSD morphology, groundwater table, and rock mass properties. As a result, the model provides a quantitative interpretation of the observed kinematic behavior of the

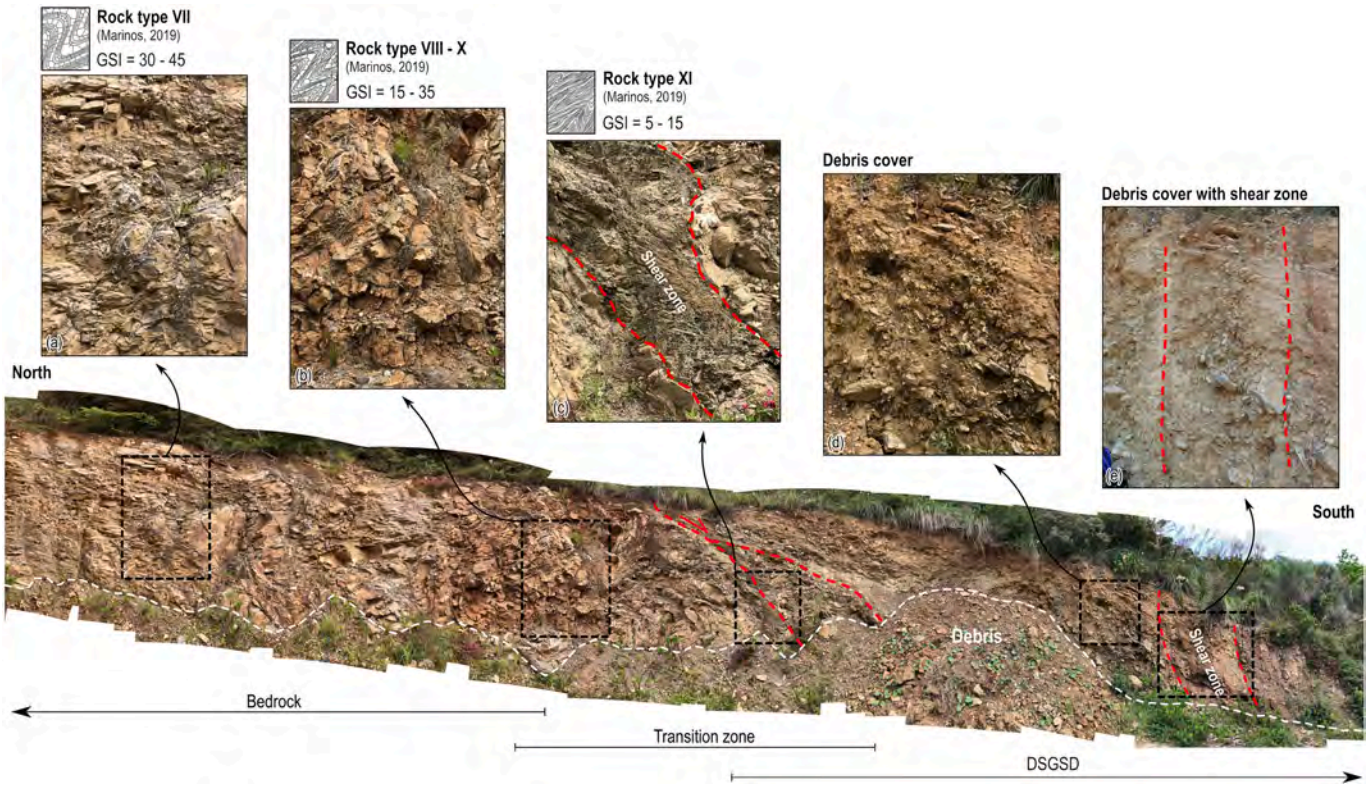

Fig. 5. Picture of the rocky front taken at the northern boundary of the DSGSD (for the location of the picture, see Fig. 4a). Panels a, b, c, d and e show a detailed view of the lithology belonging to the bedrock (a), the transition zone (b), the shear zone (c), and the top debris cover (d, e). Rock types and GSI values in panels a, b, and c are evaluated according to the scheme proposed by Marinos (2019).

DSGSD and some factors controlling the evolution of slope damage, and serves as an exemplary prototype for forward modeling, offering a comprehensive representation for studying similar slopes. To account for the effect of groundwater table in the slope stability, we considered two extreme scenarios: one with a dry slope (Model 1) and the other with a saturated slope (Model 2), assuming a groundwater table positioned at the highest recorded elevation from piezometric measurements. The viscous behavior of the rock mass involved by DSGSD is not explicitly modeled. Instead, we provide an estimate of the deformation pattern due to a potential failure related to a progressive reduction of material strength, representative of the long-term evolution of the DSGSD, by introducing a strain softening behavior for the DSGSD mass to simulate the decrease in rock mass strength caused by accumulated shear strains and the consequent development of damage and discrete shear bands (detailed information regarding the modeling approach and calibration can be found in section 1.5 in the supplementary material). The results of the analysis were interpreted within the framework of slope evolution, focusing on the spatial distribution of deformation rather than its amplitude (Apuani et al., 2013; Donati et al., 2020; Guerriero et al., 2021).

3. Results and discussion

In this section, we present a comprehensive description of the current morphological characteristics of the DSGSD, including an overview of the involved lithologies. To support our analysis, we utilize geomechanical and laboratory data that provide insights into the properties of the materials comprising the DSGSD. Additionally, we delve into the interpretation of monitoring results obtained from ground-based and remote sensing data to elucidate the long- and short-wavelength kinematic behavior of the DSGSD.

Furthermore, we conduct a detailed examination of the geometry and kinematics of the DSGSD. To achieve this, we employ both analytical and numerical approaches, which allow us to evaluate the factors influencing its kinematics. By integrating these findings, we construct an evolutionary model that encompasses the observed timespan of the DSGSD.

3.1. Current geomorphological and lithological setting of the DSGSD

The analyzed phenomenon shows many distinctive characteristics of large-scale deformation processes (Fig. 4) (Discenza and Esposito, 2021). Although the slope is not characterized by particularly steep slopes (approximately 18°-19°), the relief energy is quite high, with a maximum height of about 210 m, from the top (235 m a.s.l.) to the valley floor (25 m a.s.l.) and sufficient for the development of this type of phenomena. Its boundaries are not always well defined (especially on the northern flank), while the deformation mechanisms appear rather complex and closely connected to the geological-structural setting of the slope. Therefore, it can be classified as DSGSD (Discenza and Esposito, 2021; Jarman and Harrison, 2019).

Indeed, the gravity-induced deformation has a considerable depth and extends over the entire ridge-slope-valley floor system, producing many features typical of DSGSDs processes. The upper portion of the slope shows a well-defined, arcuated morphological scarp with a maximum height of some meters and a vertical throw of about 20 m (Fig. 4b and supplementary video V1). The scarp is affected by widespread erosional processes and is associated with morphological features such as secondary scarps, fissures, and tension cracks, which underline the planar-altimetric trend. Down the main scarp, an extended uphill-facing scarp is present. This element shows a height of some decimeters up to 1–2 m, highlighting a slightly compound mechanism in the upper part of the gravitational deformation (Hutchinson, 1989). Many longitudinal and transversal trenches, tension cracks, secondary scarps, and fissures are present in this sector (Fig. 4a).

In the middle sector, the northern and southern flanks of the DSGSD

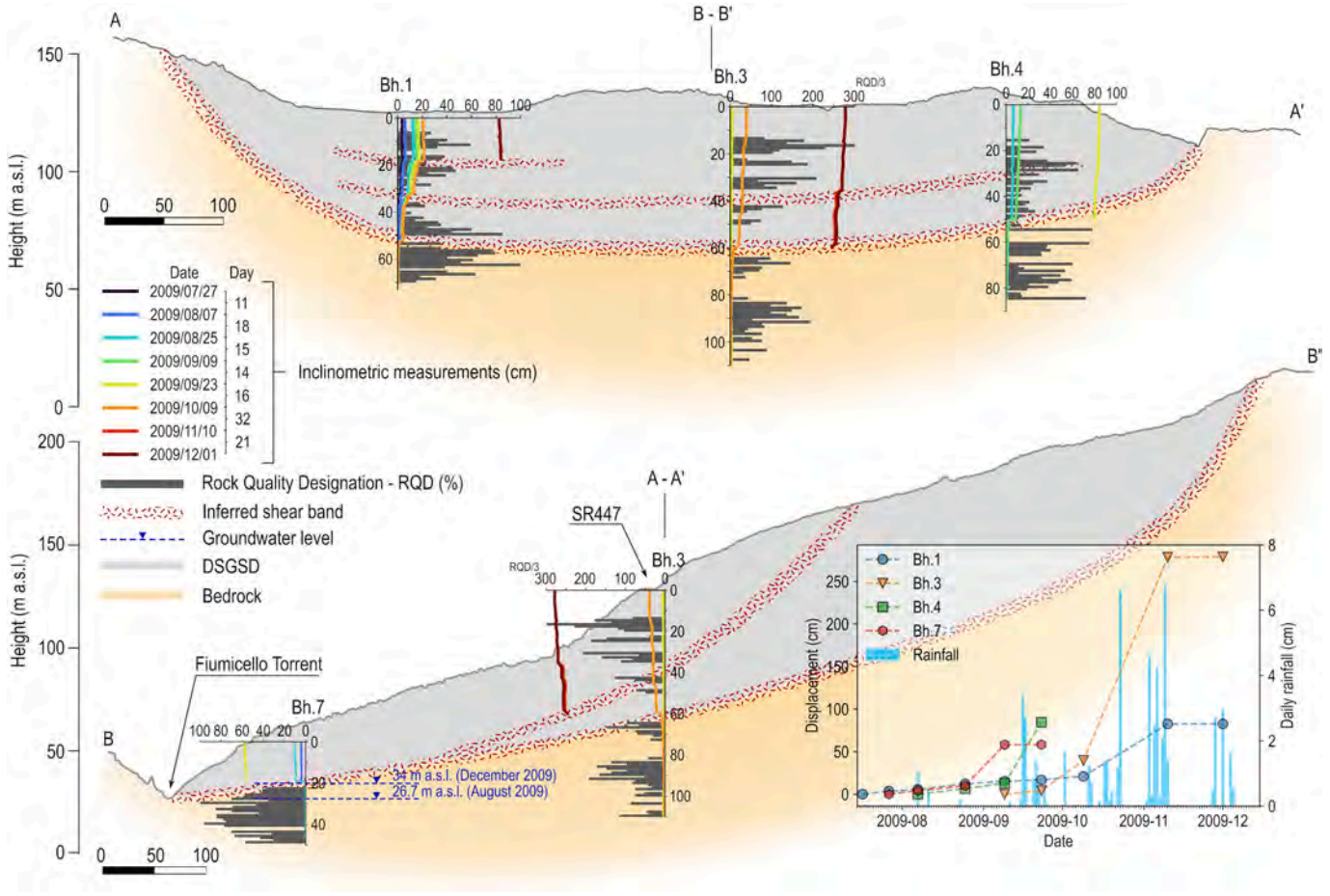

Fig. 6. Cross-sections along the A-A' and B-B′ profiles in Fig. 4a, showing the resultant displacements from inclinometric measurements and the RQD percentage with depth for each available borehole. The chart shows the trend of resultant horizontal displacements at the top of each borehole and the daily cumulated rainfall.

show different features. The northern boundary is barely visible and is marked by a series of shear planes, secondary scarps, and tension cracks of limited extension, often covered by detrital deposits, which mark a poorly defined WNW-ESE trending trench. Instead, the southern flank shows a great morpho-evolutionary tendency, characterized by two well-defined high and extended scarps defining wide and continuous WSW-ENE trending trenches with associated secondary scarps and tension cracks.

The central portion of the slope presents many morphological features with a very complex arrangement. Several wide and arcuate secondary scarps associated with the main shear planes of the DSGSD are located above the SR447 road, often accompanied by longitudinal and transversal trenches, tension cracks, and fissures with a general SW-NE trending.

The middle-lower portion of the DSGSD exhibits a distinctive convex shape, bulging outwards. This region is characterized by multiple scarps, which are limited in their extent, as well as longitudinal and transversal shear planes, fissures, and tension cracks. These geological features are often associated with shallow mass movements. This sector also displays several shallow landslides and slope instabilities, primarily occurring in areas covered by loose debris and in the uppermost weathered portions of the bedrock. Specifically, two large complex landslides, reaching a maximum thickness of approximately 20–25 m, can be found in the central and northern parts of the DSGSD.

Many tectonic elements are present in the study area (Martelli et al., 2016), such as normal and inverse faults with variable features and orientation, deforming the bedrock lithologies along extended, highly fragmented, cataclastic zones. The main faults develop approximately in the NNE-SSE direction along the *Fiumicello* Torrent valley floor. Some normal faults elongated in the N-S direction are present on the slope affected by the DSGSD. The only inverse faults develop in the NNE-SSE direction from the Tyrrhenian coast to the main deformation scarp.

Bedrock turbidites show a monoclinal west-dipping setting, often complicated by micro- and mesoscale disharmonic, tight, and isoclinal folds (Vitale et al., 2011). They consists of medium-fine sandstones and calcarenites, arranged into thin to thick layers, sometimes with lists and flint nodules, alternating with argillite mudrocks, thinly laminated and strongly tectonized (Fig. 4c and Fig. 5). In areas less affected by folding, the calcarenitic strata dip both to N-NE and SW. They are crosscut by low-angle (25° to 45°) to high-angle fractures (55° to 90°) distributed in different sets, striking mainly NW-SE (inset in Fig. 4a). Few open fractures (1–3 cm of fracture spacing) dipping more than 60° also affect these lithologies. The rock mass presents calcite and quartz veins, disharmonic tight isoclinal folds, with evidence of superpositioning, transposition, and boudinage, with increasing argillites at the fold hinge. The pelitic fraction decreases in favor of the arenaceous one in the lower portion of the sequence, consequently increasing fragile tectonic structures.

A representative picture of the structural and lithological features of the turbiditic sequence, inside and outside the DSGSD, is provided by the rocky front in Fig. 5, taken at the northern boundary of the DSGSD (Fig. 4a). Outside the DSGSD (left part in Fig. 5), the turbiditic sequence is strongly folded and jointed. It is characterized by a predominant lithoid component (Fig. 5a), with a ratio between the lithic (sandstones, calcarenites, and calcilutites) and mudrock up to 5:1–10:1 (De Vita et al., 2013). The Geological Strength Index (*GSI*), defined for

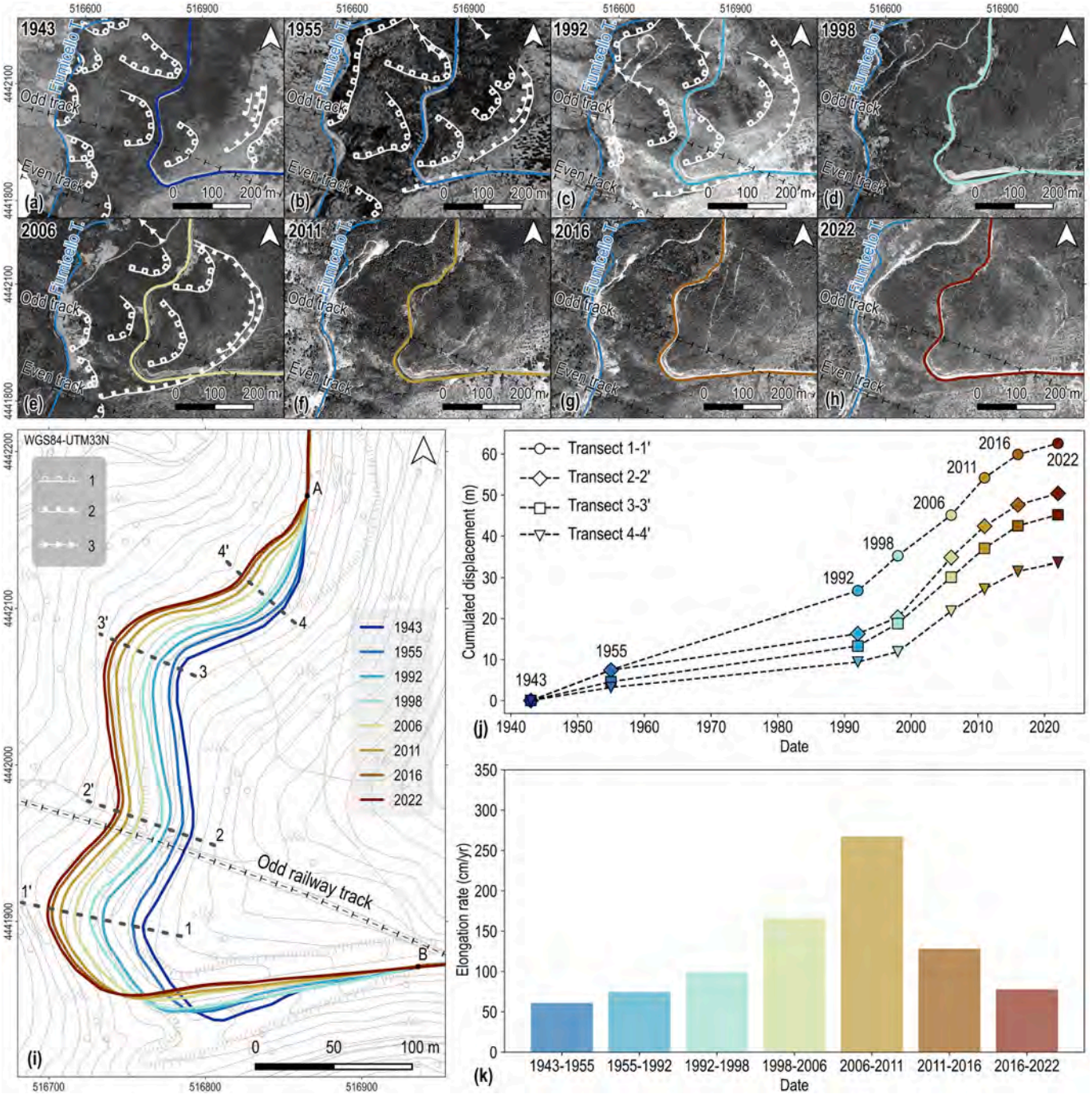

Fig. 7. Morphological analysis of the DSGSD based on stereoscopic images and spatial analysis of the SR447 road movements through orthorectified photos between 1943 and 2022 (panels a to h). (i) Evolution of the road shift towards the *Fiumicello* Torrent. (j) Cumulative horizontal displacements of the SR447 road estimated at four transects as in panel (i). (k) Elongation rate of the SR447 road estimated between points A and B in panel i, compared with the cumulated rainfall from 2006 to 2022. Key to the legend in panel i: 1. DSGSD main escarpment; 2. Secondary escarpment; 3. Localized erosion.

heterogeneous rock masses according to Marinos (2019), ranges between 30 and 45 (Rock type VII). Folding, fracturing, and mudrock percentage increase moving towards the DSGSD body (Fig. 5b), reaching lithic to mudrock ratios of about 2:1–1:1 (De Vita et al., 2013) and *GSI* values between 15 and 35 (Rock type VIII-X). Here (Fig. 5), the turbiditic succession is displaced by a marked shear zone made of a chaotic structure of strongly sheared clayey shales and mudrocks classifiable as type XI rock with a *GSI* index between 5 and 15. This shear zone displaces the whole DSGSD and contacts the lithoid mass with massive deposits of lithic elements mixed with a yellowish-brown terrigenous matrix of silt and clay (Fig. 5d), often sheared by secondary shear zones (Fig. 5e).

Bedrock along the slope is covered by coarse, poorly graded detrital and colluvial Holocene deposits, more abundant in the lower relief portion. Along the *Fiumicello* Torrent valley floor, coarse and heteromeric Holocene fluvial sediments are present, while a few meters above the riverbed, terraced and poorly graded Upper Pleistocene fluvial deposits outcrop.

The available boreholes from the 2009 survey (Italferr S.p.A, 2013c) (Fig. 4) crosscut the whole DSGSD body (Fig. 6). They identify a surficial debris cover, up to 20 m tick. Laboratory tests on samples taken at different depth classify this lithology as an heteromeric gravel with

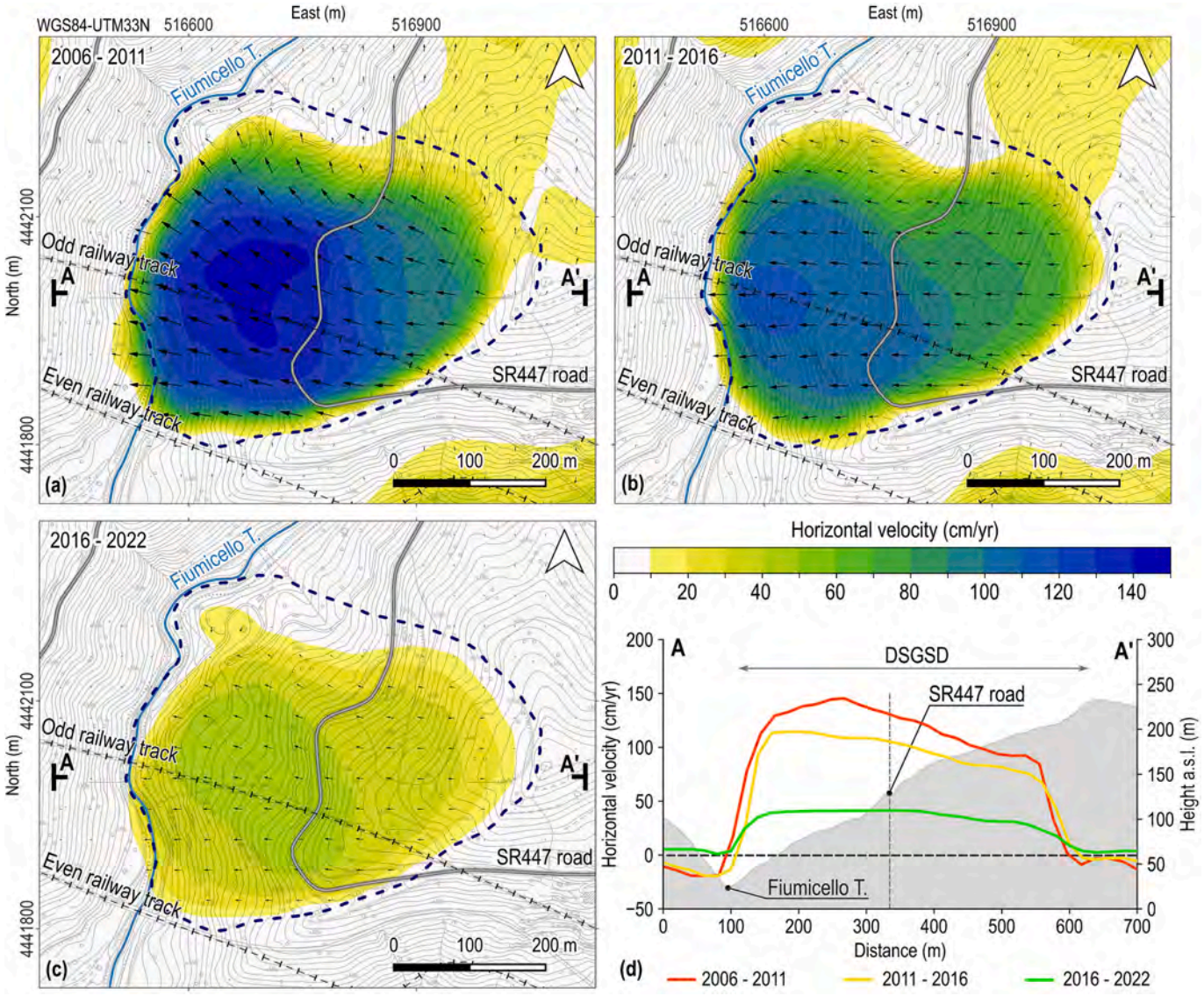

Fig. 8. Results of the DIC analysis performed on the available digital orthophotos in the period 2006–2011 (a), 2011–2016 (b), and 2016–2022 (c), expressed as mean horizontal velocities. The black arrows indicate the direction and orientation of the horizontal movements, while the dashed blue curve identifies the inferred DSGSD boundary. (d) Horizontal velocity profiles along the A-A' cross-section in panels a, b, and c for the three investigated periods. The grey area identifies the slope topography from Lidar 2008 data. (For interpretation of the references to colour in this figure legend, the reader is referred to the web version of this article.)

calcarenitic and calcareous clasts, angular to subangular in shape, immersed in a clayey, silty clayey, or weakly silty-sandy matrix, passing at depth to weak silty clay with heteromeric gravel (see supplementary Fig. S4a and Fig. 6). The debris cover passes at depth to decametric to metric levels of lithoid marly limestones and calcarenites, alternating with marls and mudrocks (De Vita et al., 2013). The average Rock Quality Designation (RQD) percentage from all the boreholes (Fig. 6) indicates that this lithology is highly weathered (RQD < 50%), with extreme values ranging from 0% (indicating very poor rock) to 90–100% (indicating excellent rock). Uniaxial compressive tests and Point Load tests conducted on samples of calcarenites and mudrocks (supplementary Fig. S4c) reveal a median uniaxial compressive strength (UCS) of 75 MPa (indicating medium strength) and 5.1 MPa (indicating very weak strength), respectively. These strength values remain relatively consistent regardless of the depth (supplementary Fig. S4c), highlighting the inherent weakness of the mudrock component.

Finally, the available piezometric data at boreholes n. 6, 2 and 5 (Fig. 4) show that only a limited section of the DSGSD toe is completely saturated by water. Specifically, borehole n.6, indicates a groundwater table ranging from 26.7 to 34 m a.s.l. in August 2009 and December 2009, respectively, as depicted in Fig. 6. On the other hand, the other two piezometers situated at boreholes number 2 and 5 (Fig. 4) did not register any groundwater levels.

3.2. *Observed long- and short-wavelength movements of the DSGSD*

The inclinometers installed at boreholes n.1, 3, 4, and 7 (Fig. 4) (Italferr S.p.A, 2013d) provided a first short-wavelength (i.e., weekly to monthly) picture of the spatial and temporal behavior of the DSGSD (Fig. 6 and supplementary Fig. S6). They identified several shear bands, several meters tick, crosscutting the lithoid mass at depths where the RQD percentage falls at values lower than 25% (Fig. 6). The inclinometers in the middle sector of the DSGSD (Bh. n. 1, 3, and 4 in Fig. 6 and supplementary Fig. S6) identify at least two shear bands approximately at 30–40- and 50–60-m depth. The inclinometer n°1 identified a further shallower shear band at about 20 m depth, probably related to a local sliding. At the DSGSD toe, the inclinometer n°7 identified a single shear band only, at approximately 20-m depth, where the debris cover

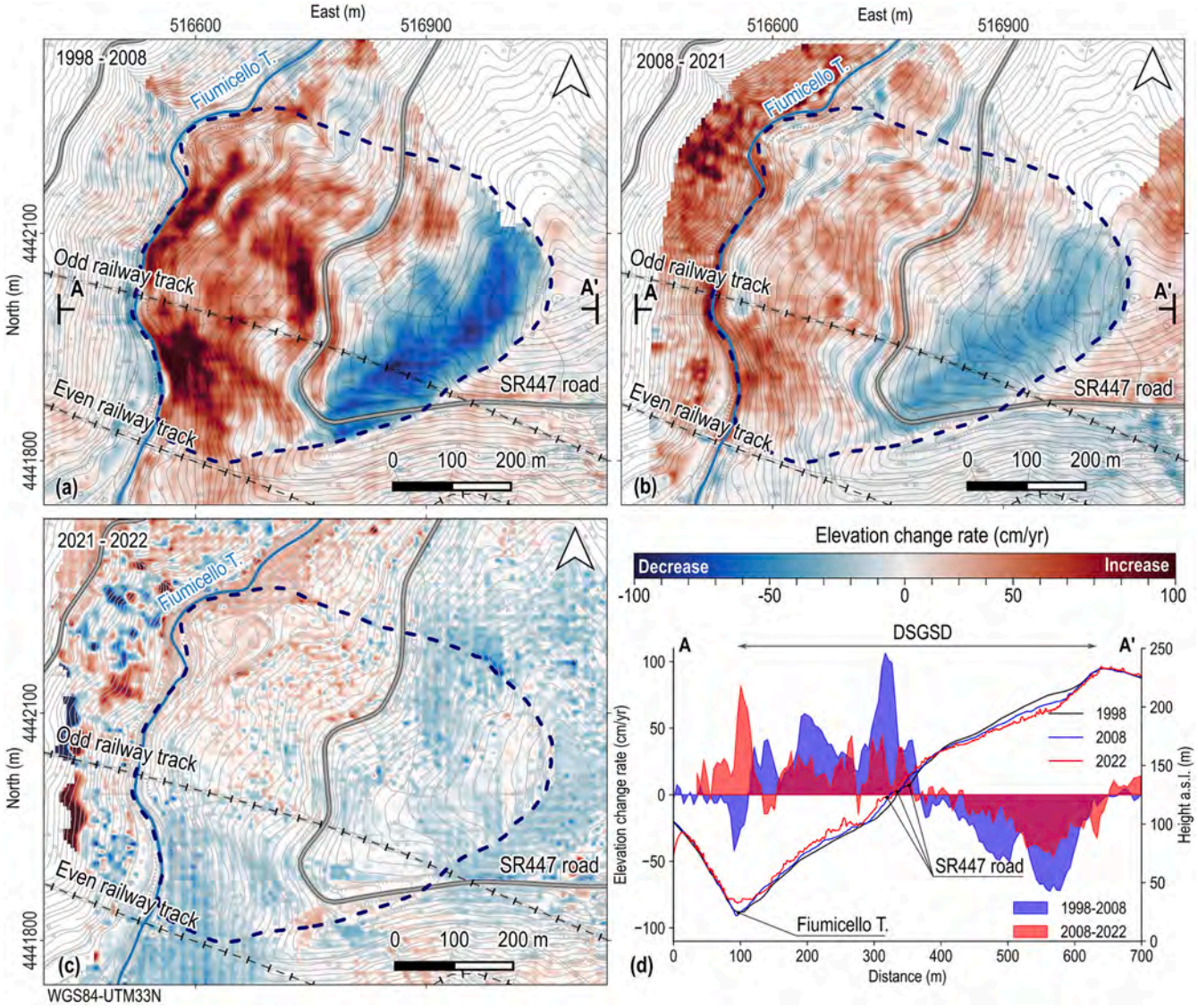

Fig. 9. Results of the DEM difference, expressed as mean elevation change rate in the period 1998–2008 (a), 2008–2021 (b), and 2021–2022 (c). (d) Elevation change rate profiles along the A-A' cross-section (panels a and b) for the 1998–2008 and 2008–2021 periods, with topographic profiles in 1998, 2008, and 2022.

switches to the altered bedrock, meaning that all the shear bands probably converge while approaching the DSGSD toe.

The resultant horizontal displacements at the ground surface (see the chart in Fig. 6), compared with the available daily rainfall data in the same period, show constant WNW-oriented displacement rates ranging between 50 and 150 cm/yr, marked by abrupt shifts up to 290 cm in approximately one month (October 10, 2009- November 11, 2009; borehole n°3 in Fig. 6) during periods of heavy rain. Displacements are both spatially and temporally heterogeneous. In space, displacement is accommodated largely by sliding along the deeper shear band at the SW part of the DSGSD (inclinometers n.3, 4, and 7 Fig. 6). In the northern part (inclinometer n.1 in Fig. 6), the higher slip is accommodated by the shallower band. Temporally, sudden accelerations due to heavy rain are not synchronous, meaning they are probably governed by changes in the saturation degree of the DSGSD mass because of rainfall infiltration (Kim et al., 2012; Zhang et al., 2018). Such results suggest that intense rainfall events may contribute to increased seepage forces and subsequent groundwater rise at the DSGSD toe, potentially influencing the acceleration of DSGSD movements. Although we have limited groundwater data, with only two measurements taken in August 2009 and December 2009, as described in par. 3.1, the correlation between rainfall and DSGSD behavior supports the hypothesis of an interaction between these factors.

A first analysis of the long-wavelength (i.e., multi-year) evolution of the DSGSD has been performed by examining the available optical dataset from 1943 to 2022 (Fig. 2). The stereoscopic analysis of historical airborne images highlighted that in 1943 the slope displayed morphologies related mostly to shallow erosional processes (Fig. 7a). However, an initial trace of the main scarp and of small secondary scarps were recognizable, highlighting that a DSGSD at its embryonic state was acting at that period. In 1955 (Fig. 7b), the main scarp expanded to the south-west, assuming a more arcuate shape and increasing its morphological impact on the slope, with the development of more accentuated secondary scarps and the growth of denudational processes in the middle part of the slope. In successive years (1990 and 2003 in Fig. 7c and e), the morphological impact of the main scarp increased further, delineating the deformational boundaries as discrete structures with the growth of its vertical throw and a further expansion to the southwest. Secondary scarps and linear cracks with strike-slip kinematics became more visible in the middle and lower sectors of the DSGSD, thus suggesting that slope displacement rates increased substantially and involved a more extensive and deeper sliding mass.

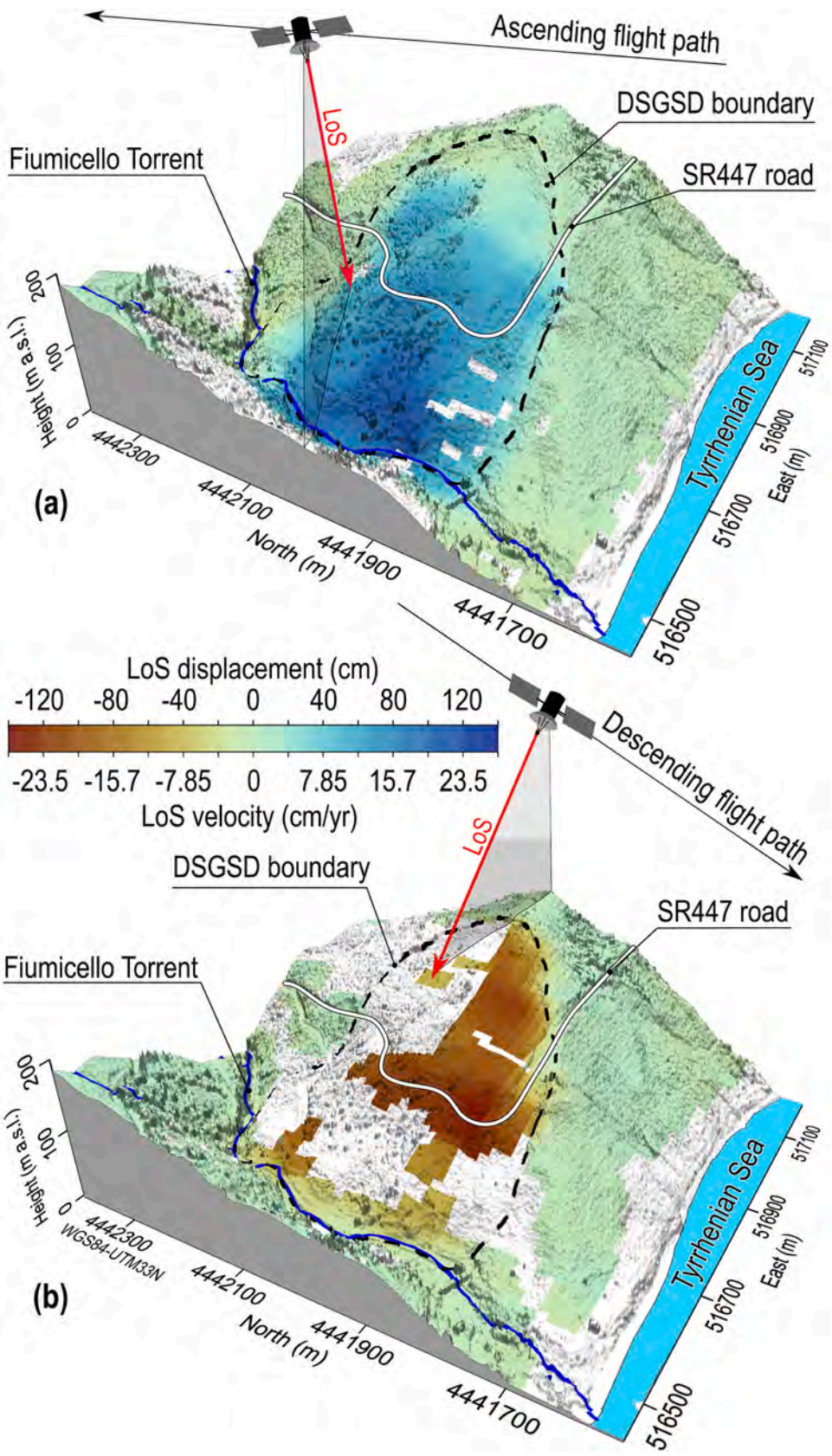

Fig. 10. Cumulated InSAR LoS displacement pattern and mean velocities between September 2016–October 2021 computed along the ascending (a) and descending (b) orbit. Negative LoS displacements indicate ground movements away from the satellite sensor, while positive LoS displacements imply ground movements approaching the satellite sensor. The uncertainty associated with both displacement maps is approximately ±7.5 cm. The sketch of the satellite ascending and descending flight path and LoS is not in scale. The 3D base grid is taken from the 2022 DSM drone survey.

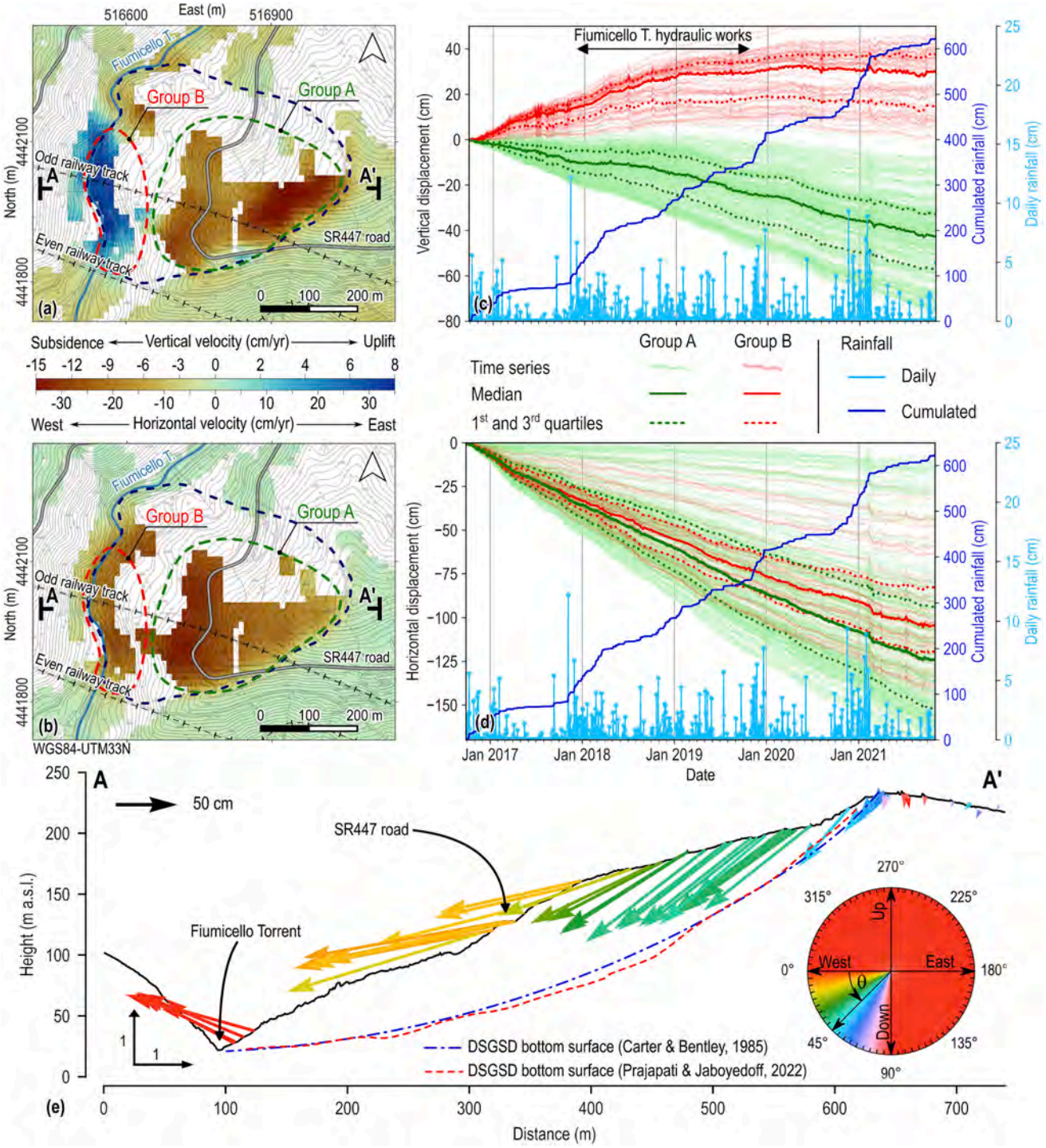

Fig. 11. Decomposition of the ascending and descending S-1 InSAR displacements between September 2016–October 2021. (a) Vertical and (b) *E*-W mean displacement rates. (c) Vertical and (d) horizontal displacement time series of the distributed scatterers inside the DSGSD boundary (the dashed blue curve in panels a and b). Group A comprises points at the top of the DSGSD, while Group B is at its toe (see panels a and b). The red and green bolded curves identify the median trend. The dotted curves correspond to the 1st and 3rd quartiles for each investigated period for Groups A and B. (e) Cumulated resultant displacement vector field on October 31, 2021, along the A-A' cross-section in panels a and b. The vector length indicates the displacement amplitude, the colour the inclination (θ). (For interpretation of the references to colour in this figure legend, the reader is referred to the web version of this article.)

The DSGSD evolution inferred from stereoscopic analysis is confirmed by the semi-quantitative investigation of its long-term horizontal movements performed by measuring the progressive shift of the SR447 road towards the *Fiumicello* Torrent, as observed from the orthorectified images available from 1943 to 2022 (Fig. 7a to h). The results (Fig. 7i) show that the road experienced metric to decametric W-NW horizontal displacements. The cumulative movement along four fixed transects perpendicular to the road axis (1–1′, 2–2′, 3–3′, 4–4′ in Fig. 7j) exhibits both temporal and spatial variations. Starting from 1992, the road experienced an acceleration, followed by a gradual deceleration from 2011 onwards. Notably, the southern part of the road (transect 1–1′) displayed larger westward displacements, reaching up to

65 m. This observation provides evidence that the DSGSD's southern flank is more dynamically active compared to its northern flank, which aligns with the morphological evidence presented in Fig. 4 and with inclinometric measurements as in Fig. 6.

To estimate the average velocity of the DSGSD, a global quantitative analysis was performed based on the elongation rate of the SR447 road, as defined in eq. (1). The results (Fig. 7k) reveal that the DSGSD experienced a progressive acceleration from 1943 to 2006, as evidenced by the increasing elongation rates, reaching its maximum velocity between 2006 and 2011. Subsequently, the velocity gradually decreased, with elongation rates in the 2016–2022 period comparable to those observed between 1943 and 1955.

The gradual deceleration of the sliding mass from 2006 onward is quantified by analyzing the horizontal movements derived from the DIC analysis of digital orthophotos spanning from 2006 to 2022 (refer to Fig. 7e to h). These maps provide a comprehensive picture of the full horizontal displacement field of the DSGSD over 16 years. The computed horizontal velocity fields during three distinct periods, i.e., 2006–2011 (Fig. 8a), 2011–2016 (Fig. 8b), and 2016–2022 (Fig. 8c), reveal that the movement encompasses the entire sliding mass, with the highest rates occurring eccentrically in the southwestern part of the DSGSD body. Notably, the horizontal movements (indicated by black arrows in Fig. 8a, b, and c) are predominantly oriented towards the west along the southern flank of the DSGSD body. As we move towards the northern side, these movements slightly rotate towards the northwest, in accordance with the change in hillslope aspect.

During the 2006–2011 period (Fig. 8a and A-A' cross-section in panel d), the maximum horizontal velocities were approximately 150 ± 10 cm/yr, corresponding to accumulated displacements of up to 7.5 ± 0.5 m. Subsequently, the velocities decreased to 115 ± 10 cm/yr (Fig. 8b and d) during the 2011–2016 period, resulting in movements of up to 5.2 ± 0.5 m. Finally, in the 2016–2022 period, the velocities further reduced to 42 ± 10 cm/yr (Fig. 8c and d), leading to displacements up to 2.6 ± 0.5 m. These findings align with the results obtained from the computed elongation ratio of the SR447 road (Fig. 7k), providing confirmation that the entire mass of the DSGSD has been gradually decelerating since 2011.

The same trend is also observed from the analysis of the available DEMs (Fig. 2), which provide a measure of the topographic height, allowing us to estimate the apparent vertical movements of the DSGSD between 1998 and 2022, expressed as mean elevation change rates. The analysis of the 1998–2008 (Fig. 9a) and 2008–2021 periods (Fig. 9b) reveals a consistent pattern. The DSGSD head experiences a decrease in altitude, the central area shows negligible or no changes, while the DSGSD toe exhibits an increase in altitude (as seen in the profiles along the A-A' section in Fig. 9d). Regarding magnitude, the elevation rates during the 1998–2008 period range from negative values up to −100 ± 8 cm/yr to positive values up to +170 ± 8 cm/yr (Fig. 9a). Between 2008 and 2021, these rates decrease to approximately −60 ± 20 cm/yr and + 80 ± 20 cm/yr (Fig. 9b). Notably, the higher elevation change observed along the *Fiumicello* Torrent during the 2008–2021 period (Fig. 9b and d) is the result of hydraulic works carried out between 2018 and 2020, which raised the height of the riverbed by up to 12 m near the odd railway tunnel. Finally, the comparison between the Drone-derived DSMs in 2021 and 2022 (Fig. 9c) reveals no significant patterns of elevation changes within the approximately seven-month time span between the two acquisitions, confirming the progressive slowdown of the DSGSD.

Finally, the InSAR multitemporal analysis offers a comprehensive picture of the recent, short-wavelength (i.e., weekly) movements of the DSGSD mass in terms of both time and space. These results encompass ground displacement maps and displacement time series measured along the satellite's Line of Sight (LoS). Examining the LoS ground displacements from September 2016 until the end of October 2021 (Fig. 10), we observe values reaching up to ±140 cm (±7.5 cm) over approximately five years, corresponding to an average rate of ±30 cm/yr. The displacements along the ascending orbit (Fig. 10a) encompass the entire DSGSD body, while the displacements along the descending orbit exhibit some blanked regions due to spatial and temporal decorrelation in the SAR signal (Fig. 10b), yet they remain confined within the DSGSD's crown and south-eastern flank. These findings provide evidence that nearly the entire DSGSD body experienced deformations during the observed time frame.

To enhance our understanding of DSGSD kinematics, we combined the LoS displacements to derive the vertical and east-west components in regions where the ascending and descending data overlap (Dalla Via et al., 2012). This decomposition assumes negligible northward movements due to the near-polar orbit of the satellite. This approximation is deemed acceptable, as supported by geomorphological investigations (Fig. 7) and DIC-derived horizontal velocities (Fig. 8), which confirm the predominant westward orientation of the DSGSD movement, particularly in its central-southern part.

The computed vertical displacement rates (Fig. 11a) reveal subsidence at the DSGSD head with rates up to -15 cm/yr, while uplift is observed at the foot with values up to +8 cm/yr. Horizontal movements (Fig. 11b) exhibit a westward orientation, reaching amplitudes of approximately −35 cm/yr. These patterns align spatially with the elevation change rates obtained from DEM difference (Fig. 9) and the horizontal displacement rates from DIC analysis (Fig. 8). Despite a direct quantitative comparison is not feasible due to the different timespan associated with the optical, elevation and SAR data, the estimated displacement rates confirm the progressive slowdown of the sliding mass. Indeed, the vertical and horizontal displacement time series of individual distributed scatterers within the DSGSD boundary (Fig. 11c and d) indicate continuous movement over time, albeit with gradually decreasing rates. The DSGSD head (Group A in Fig. 11c and d) experiences a consistent subsidence rate while moving westward with progressively lower median horizontal rates. On the other hand, the DSGSD foot (Group B in Fig. 11c and d) exhibits uplift at lower speeds until it stabilizes from 2020 onwards, approximately at the completion of the hydraulic works along the *Fiumicello* Torrent. However, westward displacements persist but gradually decrease over time.

We further combined the vertical and horizontal displacement components to determine the cumulative resultant displacement vectors along the A-A' cross-section on October 31, 2021 (Fig. 11e). At the top of the DSGSD, the vectors exhibit a downward and westward orientation with an inclination of approximately 45°-50°, indicating similar amplitudes of horizontal and vertical displacement components. In the middle of the DSGSD, the vector inclination progressively decreases to around 10°-15°, indicating an increase in the horizontal displacement amplitudes compared to the vertical ones. At the toe, the displacement vectors invert their vertical orientation from downward to upward near the *Fiumicello* Torrent, suggesting local bulging consistent with a subhorizontal, deep sliding.

From a temporal perspective (Supplementary Fig. S7 and video V2), the length of the displacement vectors, representing the displacement amplitude, gradually increases throughout the observed timespan. The vector inclination remains relatively constant, except for vectors situated in the middle of the DSGSD mass near the SR447 road. Here, the vector inclination gradually increases from approximately 0°-5° to 10°-15° starting from February–March 2019, which aligns with the completion of the *Fiumicello* Torrent refurbishment works and nearly zero vertical displacements rates at the DSGSD toe (Fig. 11c). These results suggest the presence of multiple nested shear bands within the DSGSD body, acting at different periods, and indicate that a shallower, steeper shear band accommodates the DSGSD movement in its middle part and at the toe since February–March 2019.

The displacement time series (Fig. 11c and d) exhibit slight oscillations and localized accelerations that could be attributed to variations in seasonal rainfall and extreme precipitation events. To investigate this hypothesis, we performed an additive decomposition of the vertical and horizontal displacement time series, along with the cumulative rainfall,

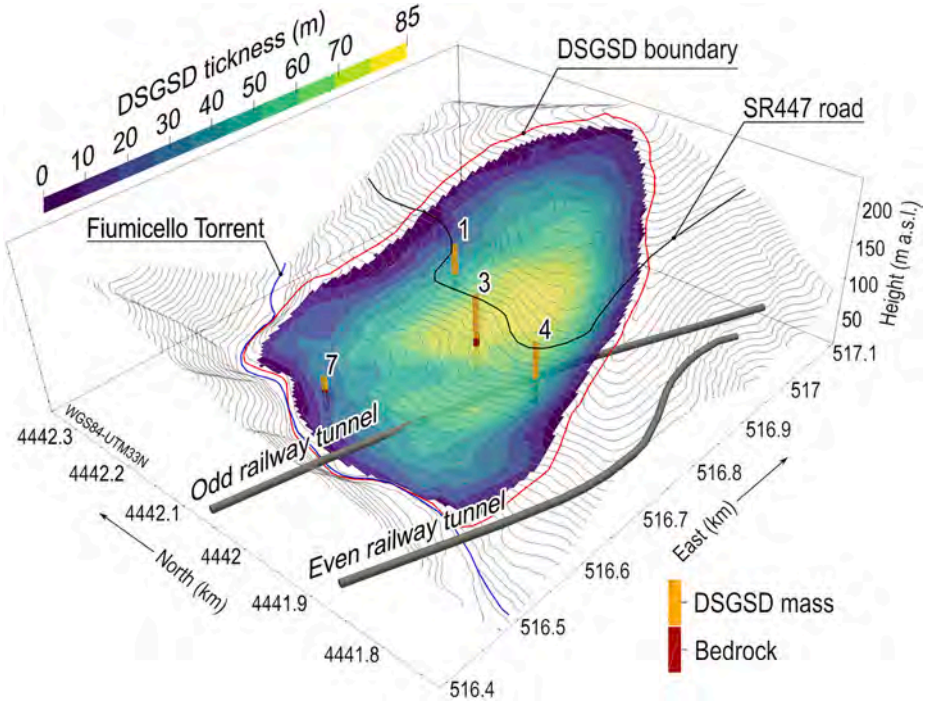

Fig. 12. 3D sketch of the DSGSD bottom surface. Contours represent the thickness of the DSGSD mass. Numbers identify the boreholes equipped with vertical inclinometers.

to analyze their trend, seasonal, and residual components. The results (supplementary Fig. S8) indicate that the trend component accounts for nearly all the observed vertical and east-west displacements, confirming the predominant influence of creep phenomena in the deformation of the displaced material. However, a secondary small-amplitude yearly seasonal signal is evident in both the vertical and east-west displacement components.

The vertical seasonal signal exhibits a phase relationship with seasonal rainfall, with subsidence slowdown corresponding to excess rainfall and vice versa. Conversely, the east-west seasonal signal is shifted by approximately three to four months relative to the seasonal rainfall, implying that excess rainfall leads to increasing westward displacements (negative values) after a delay of 3 to 4 months. This behavior could be attributed to oscillations in the groundwater table at the toe of the DSGSD, which alter the effective stresses and consequently accelerate or decelerate the movement of the DSGSD mass.

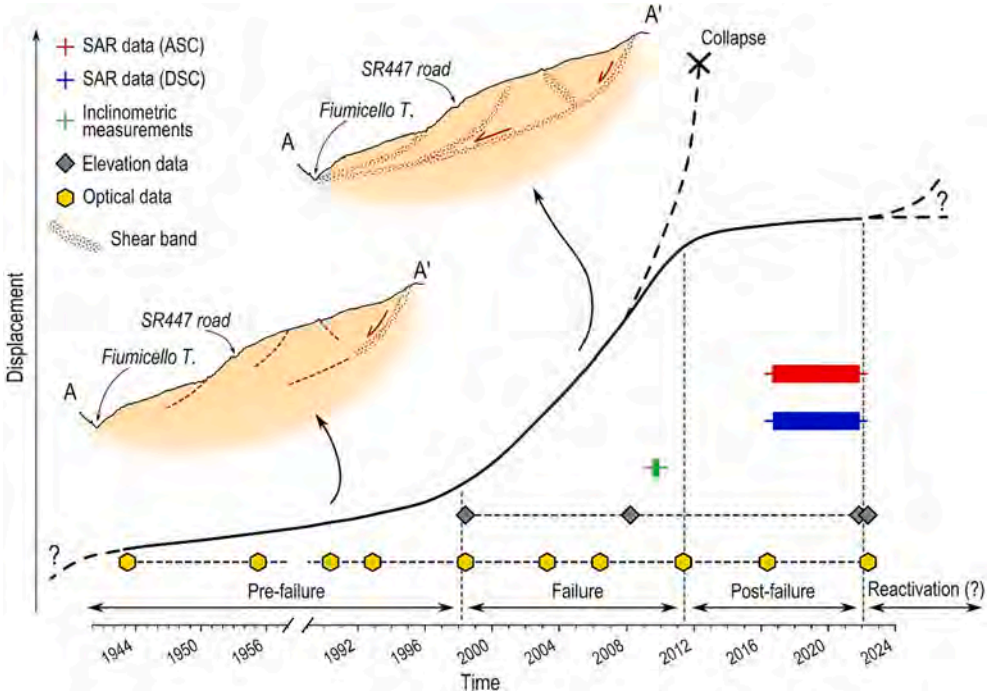

Fig. 13. Evolutionary scheme proposed for the *Pisciotta* DSGSD, together with the time coverage of the ground-based and remote sensing datasets acquired over the study area, as in Fig. 2.

3.3. Interpretation of the observed DSGSD kinematics

3.3.1. Spatial features of the DSGSD

By examining both horizontal and vertical displacements, we successfully derived the complete 3D shape and dimensions of the DSGSD mass. The boundary of the mass is depicted by the dashed blue curve in Fig. 8 through Fig. 11, encompassing an estimated area of approximately 1.8×10^5 m^2. In terms of volume, we employed the method proposed by Prajapati and Jaboyedoff (2022) (refer to section 2.4.1) to reconstruct the base of the DSGSD mass. Such an approach utilized the 2008 Lidar DTM, subsampled at a 5x5m grid, and the previously defined DSGSD boundary as input data. The resulting best fit DSGSD bottom surface is depicted in Fig. 12, along with the available vertical inclinometers, indicating the transition from the DSGSD mass to the bedrock. The Mean Absolute Error (MAE) between the observed and estimated depth of the surface is approximately 7 m. The calculated DSGSD mass exhibits a maximum thickness of about 85 m (Fig. 12) and a volume of approximately 6.2×10^6 m^3, which aligns with empirical estimates of surface area-volume relationships found in the existing literature (Guzzetti et al., 2009; Jaboyedoff et al., 2020) and with the spatial dimensions of DSGSD phenomena described in previous studies (Discenza and Esposito, 2021). Therefore, the slope moves along a compound roto-translational deep shear zone, with several secondary shallow discrete surfaces acting as secondary detachments, as testified by inclinometric measurements (Fig. 6 and supplementary Fig. S6) and by the rotation of InSAR derived displacement vectors in the central part of the slope (supplementary Video V2 and Fig. S7). Such kinematic behavior is compatible with the observed horizontal displacement patterns (Fig. 8) and justifies the observed apparent vertical collapse at the landslide head (Fig. 9), due to the opening of the landslide trench, and the height increase at its toe (Fig. 9), resulting from lateral slope motion. Moreover, the reliability of the computed bottom surface is provided by its good correspondence with the surface estimated using the Carter and Bentley (1985) method (refer to section 2.4.1). This correspondence was established by interpreting the displacement vectors derived from InSAR along the A-A' cross-section in Fig. 11e. Consequently, the computed sliding surface agrees with the observed surface displacements from InSAR data.

As expected, the odd railway track intersects the toe of the DSGSD mass for a length of approximately 60–80 m (Fig. 12), which concurs with the detected cracks in the tunnel lining as in par. 1.1 (Italferr S.p.A, 2013b).

3.3.2. Temporal behavior of the DSGSD

The available data and analysis do not provide a precise determination of the initial onset time of the DSGSD movement. Nonetheless, they offer a comprehensive insight into its kinematic behavior, spanning approximately 78 years. In accordance with the classification proposed by Leroueil and Locat (1998), slope movements can be divided into four distinct stages, as illustrated in Fig. 13.

1. Pre-failure stage: During this stage, the slope experiences strain but remains almost intact.
2. Failure stage: In this stage, a continuous surface of rupture, such as a shear band, forms within the slope and the displacement rates gradually increase until collapse.
3. Post-failure stage: This stage involves the movement of material within the landslide from the point of failure until it reaches a state of relative stability.
4. Reactivation stage: In the reactivation stage, the slope slides along preexisting shear bands. This reactivation can occur intermittently or continuously, with variations in the rate of movement over seasonal or longer time periods.

A pre-failure stage is clearly recognizable from the analysis of the 1943 and 1955 aerial images. These revealed the presence of poorly developed gravitational features, indicating a pre-existing but slightly evolved DSGSD (Fig. 7a and b). During this phase, DSGSD kinematics are governed by steady-state (secondary) creep with constant or slightly accelerating displacement rates until 1992–1998 period. Then, we observe a progressive increase in the displacement rates (Fig. 7j and k) that testifies the entry into a failure stage, probably governed by accelerating (tertiary) creep.

In the failure stage (Fig. 13), the weakening of weak rocks, along with interbedded clay-rich layers that constitute the DSGSD mass (as depicted in Fig. 5, Fig. 6, and supplementary Fig. S4), leads to the development of primary and secondary scarps, uphill-facing scarps, and linear cracks exhibiting strike-slip kinematics. These features develop at the top of the DSGSD mass and gradually extend southwestward towards the *Fiumicello* Torrent, as shown in Fig. 4 and Fig. 7a to e. Consequently, multiple discrete shear bands emerge, as indicated by inclinometric measurements (Fig. 6) and morphological analyses (Fig. 4 and Fig. 5). During this phase, two potential scenarios can unfold, as illustrated in Fig. 13: i) the displacement rate continues to increase until the landslide ultimately collapses catastrophically; ii) after an initial acceleration, the velocity diminishes, and the deforming mass reaches another stable state.

In our specific case, the *Pisciotta* DSGSD experienced its highest displacement rates between 2006 and 2011 (refer to Fig. 7j and k). However, it did not undergo catastrophic collapse. This behavior is typical of DSGSDs occurring in weak flyschoid rock masses, where the kinematics are governed by the viscous-plastic nature of clay-rich interbedded layers, leading to a ductile failure mode (Hungr et al., 2014). Consequently, we observe a gradual decline in displacement rates from 2011 to 2022, as highlighted by optical, elevation, and multitemporal InSAR data (Fig. 7j and k, Fig. 8, Fig. 9,and Fig. 11). This period can be regarded as the post-failure stage, representing the current state of the DSGSD. We anticipate a further gradual reduction in displacement rates until the DSGSD enters a phase of steady-state deformation. However, it is important to note that occasional reactivations of slope movements may still occur, potentially leading to a reactivation stage.

3.3.3. Quantitative assessment of the DSGSD kinematics

The progression from the pre-failure to post-failure stages for the *Pisciotta* DSGSD should be influenced by multiple forcing mechanisms. These mechanisms encompass upslope loading resulting from the deposition of fresh material, alterations in groundwater caused by rainfall or snowmelt, decreased shear strength from weakening and alteration, shaking induced by earthquakes, and debuttressing at the landslide toe (see Lacroix et al. (2020) and references therein). Based on the available data, there is no evidence of significant upslope loading or debuttressing occurring within the observed 78-year timeframe (see Fig. 7).

Regarding seismic activity, an analysis of the Italian Macroseismic database covering the period from 1940 to 2022 (Locati et al., 2022) revealed the occurrence of eight earthquakes with magnitudes ranging from 4 to 6.8. These seismic events resulted in macroseismic intensities ranging from 2 to 6 in the nearby municipality of *Pisciotta* (refer to supplementary Fig. S1b). According to the magnitude-distance landslide triggering chart proposed by Keefer (2002) (see supplementary Fig. S1c), it is improbable that these earthquakes would reactivate or accelerate the DSGSD, except for the Irpinia-Basilicata earthquake on November 23, 1980 (M_w 6.8). This event may have potentially contributed to the acceleration of DSGSD movements; however, it fails to explain the entirety of the observed kinematic behavior of the *Pisciotta* DSGSD. Consequently, we can exclude seismic shaking as the primary driving force during the observed period. Instead, the progressive weakening and alteration of the DSGSD material, along with changes in the groundwater regime due to rainfall, likely account for the primary mechanisms responsible for the observed kinematics of the DSGSD.

Such a hypothesis is confirmed by the results provided by the 3D

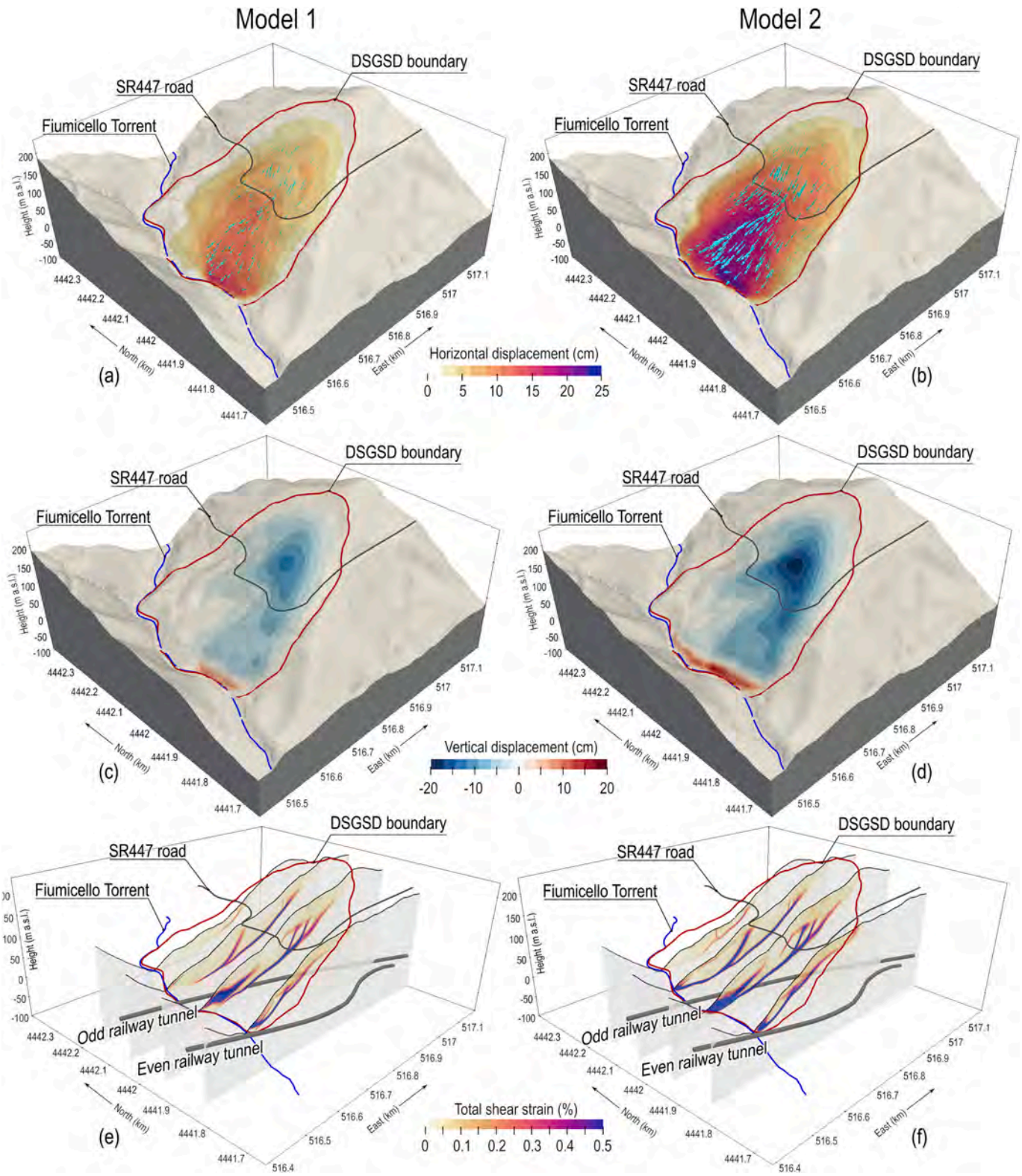

Fig. 14. Results of the numerical modeling after 30,000 numerical steps (cycles) expressed as horizontal displacements (panels a and b), vertical displacements (panels c and d) and total shear strains (panels e and f) for both Model 1 and Model 2. The blue arrows in panels a and b represent the displacement vectors. (For interpretation of the references to colour in this figure legend, the reader is referred to the web version of this article.)

numerical model of the DSGSD mass (supplementary Fig. S5) (detailed information regarding the modeling approach and calibration can be found in par. 2.4.2 and in section 1.5 in the supplementary material). Indeed (Fig. 14), both Model 1 (without groundwater table) and Model 2 (with groundwater table) exhibited horizontal (panels a and b in Fig. 14) and vertical (panels c and d in Fig. 14) displacement patterns characterized primarily by westward movements, subsidence in the upper part of the slope, and uplift at its toe, with the greatest magnitudes observed at the southwestern edge of the DSGSD. This finding agrees with observations from DIC analysis (Fig. 8), DEM height difference (Fig. 9), and

InSAR analysis (Fig. 11). Notably, the model considering the presence of a groundwater table (Model 2, supplementary Fig. S5) resulted in larger computed displacements (Fig. 14b and d). This confirms that the presence of groundwater at the toe of the DSGSD, along with its seasonal oscillations, influences the magnitude of downslope displacement rates.

The progressive weakening of the material strength caused by accumulated shear strains forms multiple shear bands at different heights, accommodating most of the computed movement, consistently with inclinometric measurements (Fig. 6 and supplementary fig. S6). In detail (panels e and f in Fig. 14), both models show a deep shear band forming at the top of the DSGSD and extending along its southwestern limit at a steep dipping angle. Further multiple shear bands develop at shallower depths, creating a complex network of surfaces with varying shapes and orientations. These shear bands converge at the DSGSD toe, forming a thick shear volume that indicates the presence of diffuse damage. Shear bands in the northern part of the DSGSD are less developed, confirming the lower activity of this sector.

The DSGSD strongly interacts with the infrastructures that crossed its path. The SR447 road experiences westward horizontal movements and subsidence, particularly at the southern edge of the DSGSD, which aligned with the movements observed in digital orthophotos (Fig. 7j and k). The even railway tunnel remains unaffected by DSGSD movements, while the odd railway tunnel intersects the DSGSD at its toe, extending at least 60–80 m to the east (supplementary Fig. S9). However, the computed DSGSD displacements near the intercepted railway section are nearly horizontal and parallel to the tunnel axis (supplementary Fig. S9). Therefore, it is hypothesized that the DSGSD mass "slides" around the tunnel walls, generating stresses compatible with the railway's operational integrity. This interpretation is supported by the limited damage to the tunnel lining observed thus far (Italferr S.p.A, 2013b) and the current functioning of both railway tracks. Furthermore, the absence of vertical displacement rates at the DSGSD toe and the steepening of InSAR-derived displacement vectors in the middle part of the DSGSD, following the completion of the *Fiumicello* Torrent hydraulic works, suggests the presence of a shallower sliding surface accommodating the current DSGSD movement, which occurs at an altitude higher than that of the tunnel.

While this work does not encompass a comprehensive assessment of the interaction between the DSGSD and the railway tunnel, the numerical model developed could serve as a forward model to gain a complete understanding of their mutual influence.

4. Conclusions

This study provided valuable insights into the intricate geometry and motion dynamics of the *Pisciotta* DSGSD, which involves complex turbiditic rock masses. By conducting a multidisciplinary analysis of an unprecedented dataset comprising geological, lithological, geomorphological, and remote sensing data (including digital orthoimages and satellite synthetic aperture radar data), we were able to unveil the nearly complete kinematic history of the DSGSD for the first time. The analysis revealed three distinct phases that characterized the behavior of the DSGSD:

- Pre-failure period: During this phase, the DSGSD experienced a gradual increase in displacement rates towards the *Fiumicello* Torrent. The analysis of available digital orthoimages identified the development and widening of various morphostructures associated with both surface and deep-seated movements.
- Failure period: In this phase, the DSGSD exhibited the highest mean displacement rates, reaching up to 150–200 cm/yr, as observed through Digital Image Correlation analysis of available digital orthophotos. Displacements were unevenly distributed across the DSGSD surface and often intensified by heavy rainfall events. The kinematics are governed by the viscous-plastic nature of clay-rich interbedded layers, leading to a ductile failure mode. The uneven distribution of these morphological features, particularly evident on the southern side of the DSGSD, and the asymmetric movement of the SR447 road highlighted the complex kinematics of the DSGSD mass. This kinematics was governed by the fragmentation of the turbiditic rock mass into interacting blocks separated by multiple shear bands.
- Post-failure period: During this phase, the DSGSD gradually decelerated its movements, with rates reaching 25–50 cm/yr. This stage was characterized by the complete development of basal and intermediate sliding surfaces within the DSGSD.

Analytical and numerical analyses of the observed DSGSD kinematics revealed its complex dynamics, including a global compound roto-translational movement, a network of deep and shallow sliding surfaces, and uneven movement distribution, especially prominent in the southern part of the DSGSD, in agreement with the morphological evidence. The observed displacement rates classified the DSGSD as an active, slow-moving rock mass, primarily influenced by viscous processes, weakening of the turbiditic succession, and changes in groundwater regime due to rainfall. The primary cause of the observed kinematics is not seismic shaking, even though it has the potential to accelerate the downward movement of the DSGSD.

Moreover, numerical modeling demonstrated the interaction between the DSGSD and interfering infrastructures, revealing that: (i) the SR447 road passively accommodates the westward movement of the DSGSD mass; (ii) the even railway remains unaffected by DSGSD movements; while (iii) the odd railway tunnel intersects the DSGSD at its base. However, DSGSD movements, nearly parallel to the tunnel axis, do not appear to pose a significant threat to the stability of the infrastructure (supplementary Fig. S9).

To enhance our understanding of the DSGSD, further investigations, monitoring, and advanced numerical modeling are necessary. These efforts should focus on evaluating the impact of meteorological factors and temporal-variable slope deformation behavior, assessing the potential instability and forecasting potential failure scenarios of the sliding mass, and comprehensively analyzing the interaction between the DSGSD and railway tunnels, considering detailed information on construction phases, geometrical features, and tunnel reinforcements.

Supplementary data to this article can be found online at https://doi.org/10.1016/j.rse.2023.113751.

CRediT authorship contribution statement

Matteo Albano: Conceptualization, Methodology, Formal analysis, Writing – original draft, Visualization. **Michele Saroli:** Conceptualization, Investigation, Writing – review & editing, Supervision. **Lisa Beccaro:** Investigation, Resources, Data curation. **Marco Moro:** Investigation, Writing – review & editing, Validation, Supervision, Project administration. **Fawzi Doumaz:** Investigation, Data curation. **Marco Emanuele Discenza:** Investigation, Resources, Writing – review & editing. **Luca Del Rio:** Investigation. **Matteo Rompato:** Investigation.

Declaration of Competing Interest

The authors declare that they have no known competing financial interests or personal relationships that could have appeared to influence the work reported in this paper.

Data availability

The geological and geomorphological maps used in this study ((i) Modello morfologico e cinematico del processo deformativo (D02201R69A7GE0003001A - scala 1:1.000); (ii) Carta Geolitologica (D02201R69N6GE0001001B - scala 1:2.000); (ii) Carta Geomorfologica (D02201R69N6GE0003001B - scala 1:2.000); (iii) Carta Geologica

integrativa (D02201R69RHGE0001001B)) are provided by Italian Railway Network - RFI S.p.A. in the framework of the agreement n. RFI-DTC.SI.GE\A0011\P\2022\0000028 of March 3, 2022 between RFI S.p.A. and INGV. The in-situ geotechnical surveys, inclinometric data, and geometrical features of the odd and even railway tracks used in this study are taken from the final draft "Ferrovia Battipaglia-Reggio C. – sottoprogetto SP13 – costruzione galleria subalvea Torrente Fiumicello", available from the Department of Economic Policy Planning and Coordination at: https://www.programmazioneeconomica.gov.it/ferrovia-battipaglia-reggio-c-sottoprogetto-sp13-costruzione-galleria-subalvea-torrente-fiumicello-progetto-definitivo/. The airborne optical images dated 1943, 1955, 1990 and 2003 are property of the Military Geographical Institute (IGM) and are provided according to the agreement n.0001094 of January 27, 2017, between IGM and INGV. Sentinel-1 SAR data are provided by the European Space Agency and are available from the Copernicus Open Access Hub (https://scihub.copernicus.eu/dhus/#/home). The DIC algorithm used in this study is available at: https://github.com/bickelmps/DIC_FFT_ETHZ. The LiDAR dataset is provided by the Geology and Geotechnologies Laboratory (INGV, http://istituto.ingv.it/it/36-laboratori/1656-laboratorio-geologia-e-geotecnologie.html) in the framework of an agreement with the Ministry of the Environment, Earth and Sea (http://www.pcn.minambiente.it) - Italian National Geoportal, owner of the data. Rainfall data are available from the Multirisk Centre of the Campania region (http://centrofunzionale.regione.campania.it/#/pages/dashboard). Ancillary data used in this study (e.g., topographic maps and linear infrastructure vector files) are available from the Campania Region Geoportal (https://sit2.regione.campania.it/node).

Acknowledgments

This work is part of the research project FRASI-MATTM "*Approccio integrato multi-scala per la definizione della pericolosità da frana sismo-indotta nel territorio italiano*", funded by the Italian Ministry of the Environment and Land and Sea Protection (now Ministry of Ecological Transition - MiTE). We thank Dr. Geol. Girolamo Dixit Dominus for the support during the first survey in October 2021 and Dr. Christian Bignami for the fruitful discussions on Digital Image Correlation analysis. RFI S.p.A. is acknowledged for providing the geomorphological maps of the study area. Views and conclusions of the study are those of the authors, and they should not be interpreted as representing official policies, either expressed or implied, of RFI S.p.A..

References

Aaron, J., Loew, S., Forrer, M., 2021. Recharge response and kinematics of an unusual earthflow in Liechtenstein. Landslides 18, 2383–2401. https://doi.org/10.1007/S10346-021-01633-5/FIGURES/15.

Agisoft LLC, 2022. Agisoft Metashape Professional (Version 1.8.1) (software).

Agliardi, F., Crosta, G.B., Frattini, P., 2012. Slow rock-slope deformation. In: Clague, J.J., Stead, D. (Eds.), Landslides. Cambridge University Press, pp. 207–221. https://doi.org/10.1017/CBO9780511740367.019.

Agliardi, F., Scuderi, M.M., Fusi, N., Collettini, C., 2020. Slow-to-fast transition of giant creeping rockslides modulated by undrained loading in basal shear zones. Nat. Commun. 11, 1352. https://doi.org/10.1038/s41467-020-15093-3.

Allmendinger, R.W., Cardozo, N., Fisher, D.M., 2011. Structural Geology Algorithms: Vectors and Tensors, 1st ed. Cambridge University Press. https://doi.org/10.1017/CBO9780511920202.

Ambrosi, C., Crosta, G.B., 2011. Valley shape influence on deformation mechanisms of rock slopes. SP 351, 215–233. https://doi.org/10.1144/SP351.12.

Apuani, T., Corazzato, C., Merri, A., Tibaldi, A., 2013. Understanding Etna flank instability through numerical models. J. Volcanol. Geotherm. Res. 251, 112–126. https://doi.org/10.1016/j.jvolgeores.2012.06.015.

Barbarella, M., Benedetto, A.D., Fiani, M., Guida, D., Lugli, A., 2018. Use of DEMs derived from TLS and HRSI data for landslide feature recognition. ISPRS Int. J. Geo Inf. 7, 160. https://doi.org/10.3390/ijgi7040160.

Barbarella, M., Cuomo, A., Di Benedetto, A., Fiani, M., Guida, D., 2019. Topographic base maps from remote sensing data for engineering geomorphological modelling: an application on coastal mediterranean landscape, 2019 Geosciences 9. https://doi.org/10.3390/GEOSCIENCES9120500, 500 9, 500.

Barbarella, M., Fiani, M., 2013. Monitoring of large landslides by terrestrial laser scanning techniques: field data collection and processing. Eur. J. Remote Sens. 46, 126–151. https://doi.org/10.5721/EuJRS20134608.

Barbarella, M., Fiani, M., Lugli, A., 2015. Landslide monitoring using multitemporal terrestrial laser scanning for ground displacement analysis. Geomat. Nat. Haz. Risk 6, 398–418. https://doi.org/10.1080/19475705.2013.863808.

Barla, G., Paronuzzi, P., 2013. The 1963 vajont landslide: 50th anniversary. Rock Mech. Rock. Eng. 46, 1267–1270. https://doi.org/10.1007/s00603-013-0483-7.

Berardino, P., Fornaro, G., Lanari, R., Sansosti, E., 2002. A new algorithm for surface deformation monitoring based on small baseline differential SAR interferograms. IEEE Trans. Geosci. Remote Sens. 40, 2375–2383. https://doi.org/10.1109/TGRS.2002.803792.

Bickel, V.T., Manconi, A., 2022. Decadal surface changes and displacements in Switzerland. J Geovis Spat Anal 6, 24. https://doi.org/10.1007/s41651-022-00119-9.

Bickel, V.T., Manconi, A., Amann, F., 2018. Quantitative assessment of digital image correlation methods to detect and monitor surface displacements of large slope instabilities. Remote Sens. 10 https://doi.org/10.3390/RS10060865, 865 10, 865.

Bonardi, G., Ciarcia, S., Di Nocera, S., Matano, F., Sgrosso, I., Torre, M., 2009. Carta delle principali unità cinematiche dell'Appennino meridionale. Nota illustrativa. Italian J. Geosci. 128.

Caporossi, P., Mazzanti, P., Bozzano, F., 2018. Digital image correlation (DIC) analysis of the 3 december 2013 montescaglioso landslide (Basilicata, southern Italy): results from a multi-dataset investigation. IJGI 7, 372. https://doi.org/10.3390/ijgi7090372.

Carter, M., Bentley, S.P., 1985. The geometry of slip surfaces beneath landslides: predictions from surface measurements. Can. Geotech. J. 22, 234–238. https://doi.org/10.1139/t85-031.

Casagli, N., Intrieri, E., Tofani, V., Gigli, G., Raspini, F., 2023. Landslide detection, monitoring and prediction with remote-sensing techniques. Nat. Rev. Earth Environ. 4, 51–64. https://doi.org/10.1038/s43017-022-00373-x.

Casu, F., Manzo, M., Lanari, R., 2006. A quantitative assessment of the SBAS algorithm performance for surface deformation retrieval from DInSAR data. Remote Sens. Environ. 102, 195–210. https://doi.org/10.1016/J.RSE.2006.01.023.

Chalupa, V., Pánek, T., Šilhán, K., Březný, M., Tichavský, R., Grygar, R., 2021. Low-topography deep-seated gravitational slope deformation: slope instability of flysch thrust fronts (Outer Western Carpathians). Geomorphology 389, 107833. https://doi.org/10.1016/j.geomorph.2021.107833.

Chigira, M., Tsou, C.Y., Matsushi, Y., Hiraishi, N., Matsuzawa, M., 2013. Topographic precursors and geological structures of deep-seated catastrophic landslides caused by typhoon Talas. Geomorphology 201, 479–493. https://doi.org/10.1016/J.GEOMORPH.2013.07.020.

Ciarcia, S., Mazzoli, S., Vitale, S., Zattin, M., 2012. On the tectonic evolution of the ligurian accretionary complex in southern Italy. Geol. Soc. Am. Bull. 124, 463–483. https://doi.org/10.1130/B30437.1.

Crosta, G.B., di Prisco, C., Frattini, P., Frigerio, G., Castellanza, R., Agliardi, F., 2014. Chasing a complete understanding of the triggering mechanisms of a large rapidly evolving rockslide. Landslides 11, 747–764. https://doi.org/10.1007/s10346-013-0433-1.

Crosta, G.B., Frattini, P., Agliardi, F., 2013. Deep seated gravitational slope deformations in the european Alps. Tectonophysics 605, 13–33. https://doi.org/10.1016/j.tecto.2013.04.028.

Dalla Via, G., Crosetto, M., Crippa, B., 2012. Resolving vertical and east-west horizontal motion from differential interferometric synthetic aperture radar: the L'Aquila earthquake. Journal of Geophysical Research: Solid Earth 117. https://doi.org/10.1029/2011JB008689.

De Blasio, I., Lima, A., Perrone, V., Russo, M., 1978. Studio petrografico e biostratigrafico di una sezione della formazione del saraceno nell'area-tipo (Calabria Nord-orientale). Rivista Italiana di Paleontologia 84, 947–972.

De Vita, P., Carratù, M.T., Barbera, G.L., Santoro, S., 2013. Kinematics and geological constraints of the slow-moving pisciotta rock slide (southern Italy). Geomorphology 201, 415–429. https://doi.org/10.1016/J.GEOMORPH.2013.07.015.

De Vita, P., Cusano, D., La Barbera, G., 2017. Complex rainfall-driven kinematics of the slow-moving pisciotta rock-slide (Cilento, southern Italy). In: Mikoš, M., Casagli, N., Yin, Y., Sassa, K. (Eds.), Advancing Culture of Living with Landslides. Springer International Publishing, Cham, pp. 547–556. https://doi.org/10.1007/978-3-319-53485-5_64.

Deere, D.U., Deere, D.W., 1988. The Rock Quality Designation (RQD) in Practice. In: Rock Classification Systems for Engineering Purposes, ASTM STP 984. Philadelphia, pp. 91–101.

Discenza, M.E., Esposito, C., 2021. State-of-art and remarks on some open questions about DSGSDs: hints from a review of the scientific literature on related topics. Italian J. Eng. Geol.Environ. 21, 31–59. https://doi.org/10.4408/IJEGE.2021-01.O-03.

Discenza, M.E., Esposito, C., Martino, S., Petitta, M., Prestininzi, A., Scarascia Mugnozza, G., 2011. The gravitational slope deformation of mt. Rocchetta ridge (central apennines, Italy): geological-evolutionary model and numerical analysis. Bull. Eng. Geol. Environ. 70, 559–575. https://doi.org/10.1007/s10064-010-0342-7.

Discenza, M.E., Martino, S., Bretschneider, A., Scarascia Mugnozza, G., 2020. Influence of joints on creep processes involving rock masses: results from physical-analogue laboratory tests. Int. J. Rock Mech. Min. Sci. 128, 104261 https://doi.org/10.1016/j.ijrmms.2020.104261.

Donati, D., Stead, D., Stewart, T.W., Marsh, J., 2020. Numerical modelling of slope damage in large, slowly moving rockslides: insights from the downie slide, British

Columbia,Canada. Eng. Geol. 273, 105693 https://doi.org/10.1016/j.enggeo.2020.105693.
Esposito, C., Di Luzio, E., Baleani, M., Troiani, F., Della Seta, M., Bozzano, F., Mazzanti, P., 2021. Fold architecture predisposing deep-seated gravitational slope deformations within a flysch sequence in the northern apennines (Italy). Geomorphology 380, 107629. https://doi.org/10.1016/j.geomorph.2021.107629.
Falcone, S., 2023. Stereoscopia 1.0.0. https://doi.org/10.5281/ZENODO.7515318.
Guerriero, L., Prinzi, E.P., Calcaterra, D., Ciarcia, S., Di Martire, D., Guadagno, F.M., Ruzza, G., Revellino, P., 2021. Kinematics and geologic control of the deep-seated landslide affecting the historic center of buonalbergo, southern Italy. Geomorphology 394, 107961. https://doi.org/10.1016/j.geomorph.2021.107961.
Guzzetti, F., Ardizzone, F., Cardinali, M., Rossi, M., Valigi, D., 2009. Landslide volumes and landslide mobilization rates in Umbria, Central Italy. Earth Planet. Sci. Lett. 279, 222–229. https://doi.org/10.1016/J.EPSL.2009.01.005.
Hungr, O., Leroueil, S., Picarelli, L., 2014. The varnes classification of landslide types, an update. Landslides 11, 167–194. https://doi.org/10.1007/s10346-013-0436-y.
Hutchinson, J.N., 1989. General report: morphological and geotechnical parameters of landslides in relation to geology and hydrogeology. Int. J. Rock Mech. Min. Sci. Geomech. Abstracts 26, 88. https://doi.org/10.1016/0148-9062(89)90310-0.
Isenburg, M., 2021. LAStools - efficient tools for LiDAR processing (version 111216).
Italferr S.p.A, 2013. Opere civili: relazione stato di fatto, Adeguamenti linea ferroviaria tirrenica Battipaglia-Reggio Calabria. Costruzione della galleria subalvea Fiumicello - Progetto definitivo. Available at: https://www.programmazioneeconomica.gov.it/ferrovia-battipaglia-reggio-c-sottoprogetto-sp13-costruzione-galleria-subalvea-torrente-fiumicello-progetto-definitivo/.
Italferr S.p.A, 2013. Geologia: interventi di consolidamento, Adeguamenti linea ferroviaria tirrenica Battipaglia-Reggio Calabria. Costruzione della galleria subalvea Fiumicello - Progetto definitivo. Available at: https://www.programmazioneeconomica.gov.it/ferrovia-battipaglia-reggio-c-sottoprogetto-sp13-costruzione-galleria-subalvea-torrente-fiumicello-progetto-definitivo/.
Italferr S.p.A, 2013. Geologia: Relazione tecnica specialistica geotecnica, Adeguamenti linea ferroviaria tirrenica Battipaglia-Reggio Calabria. Costruzione della galleria subalvea Fiumicello - Progetto definitivo. Available at: https://www.programmazioneeconomica.gov.it/ferrovia-battipaglia-reggio-c-sottoprogetto-sp13-costruzione-galleria-subalvea-torrente-fiumicello-progetto-definitivo/.
Italferr S.p.A, 2013. Geologia: relazione dati di monitoraggio, Adeguamenti linea ferroviaria tirrenica Battipaglia-Reggio Calabria. Costruzione della galleria subalvea Fiumicello - Progetto definitivo. Available at: https://www.programmazioneeconomica.gov.it/ferrovia-battipaglia-reggio-c-sottoprogetto-sp13-costruzione-galleria-subalvea-torrente-fiumicello-progetto-definitivo/.
Italferr S.p.A, 2011. Carta geolitologica (D02201R69N6GE0001001B - scala 1:2.000), Intervento di messa in sicurezza della Linea Salerno-Reggio Calabria tra le località di Ascea e Pisciotta in Provincia di Salerno - Integrazione al progetto preliminare.
Italferr S.p.A, 2011. Carta Geomorfologica (D02201R69N6GE0003001B - scala 1:2.000), Intervento di messa in sicurezza della Linea Salerno-Reggio Calabria tra le località di Ascea e Pisciotta in Provincia di Salerno - Integrazione al progetto preliminare.
Italferr S.p.A, 2011. Carta Geologica integrativa (D02201R69RHGE0001001B), Intervento di messa in sicurezza della Linea Salerno-Reggio Calabria tra le località di Ascea e Pisciotta in Provincia di Salerno - Integrazione al progetto preliminare.
Jaboyedoff, M. (Ed.), 2011. Slope tectonics, Geological Society special publication. Geological Society; Distributors, North America, for trade and institutional orders, Geological Society, c/o AIDC. Williston, VT, London.
Jaboyedoff, M., Carrea, D., Derron, M.-H., Oppikofer, T., Penna, I.M., Rudaz, B., 2020. A review of methods used to estimate initial landslide failure surface depths and volumes. Eng. Geol. 267, 105478 https://doi.org/10.1016/j.enggeo.2020.105478.
Jarman, D., Harrison, S., 2019. Rock slope failure in the british mountains. Geomorphology 340, 202–233. https://doi.org/10.1016/j.geomorph.2019.03.002.
Keefer, D.K., 2002. Investigating landslides caused by earthquakes - a historical review. Surv. Geophys. 23, 473–510.
Kim, J., Jeong, S., Regueiro, R.A., 2012. Instability of partially saturated soil slopes due to alteration of rainfall pattern. Eng. Geol. 147–148, 28–36. https://doi.org/10.1016/j.enggeo.2012.07.005.
Lacroix, P., Handwerger, A.L., Bièvre, G., 2020. Life and death of slow-moving landslides. Nat. Rev. Earth Environ. 1, 404–419. https://doi.org/10.1038/s43017-020-0072-8.
Lanari, R., Casu, F., Manzo, M., Zeni, G., Berardino, P., Manunta, M., Pepe, A., 2007. An overview of the small BAseline subset algorithm: a DInSAR technique for surface deformation analysis. In: Deformation and Gravity Change: Indicators of Isostasy, Tectonics, Volcanism, and Climate Change, 637–661. https://doi.org/10.1007/978-3-7643-8417-3_2.
Leroueil, S., Locat, J., 1998. Slope movements — Geotechnical characterization, risk assessment and mitigation. In: Presented at the 8th International IAEG Congress. CRC Press, Balkema, Rotterdam, pp. 95–106. https://doi.org/10.1201/9781003078173-6.
Livio, F.A., Zerboni, A., Ferrario, M.F., Mariani, G.S., Martinelli, E., Amit, R., 2022. Triggering processes of deep-seated gravitational slope deformation (DSGSD) in an un-glaciated area of the Cavargna Valley (Central southern Alps) during the middle holocene. Landslides 19, 1825–1841. https://doi.org/10.1007/s10346-022-01892-w.
Locati, M., Camassi, R., Rovida, A., Ercolani, E., Bernardini, F., Castelli, V., Caracciolo, C. H., Tertulliani, A., Rossi, A., Azzaro, R., D'Amico, S., Antonucci, A., 2022. Database Macrosismico Italiano (DBMI15), versione 4.0. https://doi.org/10.13127/DBMI/DBMI15.4.
Mansour, M.F., Morgenstern, N.R., Martin, C.D., 2011. Expected damage from displacement of slow-moving slides. Landslides 8, 117–131. https://doi.org/10.1007/s10346-010-0227-7.
Marinos, V., 2019. A revised, geotechnical classification GSI system for tectonically disturbed heterogeneous rock masses, such as flysch. Bull. Eng. Geol. Environ. 78, 899–912. https://doi.org/10.1007/s10064-017-1151-z.
Martelli, L., Nardi, G., Cavuoto, G., Conforti, A., Ferraro, L., D'Argenio, B., 2016. Note illustrative della Carta Geologica d'Italia alla scala 1:50.000; foglio 519 Capo Palinuro. Istituto Superiore per la Protezione e la Ricerca Ambientale, Regione Campania.
Moro, M., Chini, M., Saroli, M., Atzori, S., Stramondo, S., Salvi, S., 2011. Analysis of large, seismically induced, gravitational deformations imaged by high-resolution COSMO-SkyMed synthetic aperture radar. Geology 39, 527–530. https://doi.org/10.1130/G31748.1.
Notti, D., Wrzesniak, A., Dematteis, N., Lollino, P., Fazio, N.L., Zucca, F., Giordan, D., 2021. A multidisciplinary investigation of deep-seated landslide reactivation triggered by an extreme rainfall event: a case study of the monesi di mendatica landslide, ligurian Alps. Landslides 18, 2341–2365. https://doi.org/10.1007/s10346-021-01651-3.
Pánek, T., Klimeš, J., 2016. Temporal behavior of deep-seated gravitational slope deformations: a review. Earth Sci. Rev. 156, 14–38. https://doi.org/10.1016/j.earscirev.2016.02.007.
Pedrazzini, A., Jaboyedoff, M., Loye, A., Derron, M.-H., 2013. From deep seated slope deformation to rock avalanche: destabilization and transportation models of the Sierre landslide (Switzerland). Tectonophysics 605, 149–168. https://doi.org/10.1016/j.tecto.2013.04.016.
Prajapati, G., Jaboyedoff, M., 2022. Method to estimate the initial landslide failure surface and volumes using grid points and spline curves in MATLAB. Landslides 19, 2997–3008. https://doi.org/10.1007/s10346-022-01940-5.
QGIS Development Team, 2022. QGIS Geographic Information System ver. 3.22.
Raack, J., Conway, S.J., Heyer, T., Bickel, V.T., Philippe, M., Hiesinger, H., Johnsson, A., Massé, M., 2020. Present-day gully activity in sisyphi cavi, Mars – flow-like features and block movements. Icarus 350, 113899. https://doi.org/10.1016/J.ICARUS.2020.113899.
Rovida, A., Locati, M., Camassi, R., Lolli, B., Gasperini, P., Antonucci, A., 2022. Catalogo Parametrico dei Terremoti Italiani (CPTI15), versione 4.0. https://doi.org/10.13127/CPTI/CPTI15.4.
Sarmap, 2021. SARscape® v5.6.0-User Guide. Purasca, Switzerland.
Saroli, M., Albano, M., Atzori, S., Moro, M., Tolomei, C., Bignami, C., Stramondo, S., 2021. Analysis of a large seismically induced mass movement after the december 2018 Etna volcano (southern Italy) seismic swarm. Remote Sens. Environ. 263, 112524 https://doi.org/10.1016/j.rse.2021.112524.
Storni, E., Hugentobler, M., Manconi, A., Loew, S., 2020. Monitoring and analysis of active rockslide-glacier interactions (Moosfluh, Switzerland). Geomorphology 371, 107414. https://doi.org/10.1016/J.GEOMORPH.2020.107414.
Stucchi, M., Meletti, C., Montaldo, V., Crowley, H., Calvi, G.M., Boschi, E., 2011. Seismic Hazard assessment (2003–2009) for the italian building code. Bull. Seismol. Soc. Am. 101, 1885–1911. https://doi.org/10.1785/0120100130.
Vezzani, L., 1968. Distribuzione, facies e stratigrafia della Formazione del Saraceno (Albiano-Daniano) nell'area compresa tra il Mare Jonio ed il Torrente Frido. Geologica Rmana 7, 229–276.
Vitale, S., Ciarcia, S., Mazzoli, S., Zaghloul, M.N., 2011. Tectonic evolution of the 'Liguride' accretionary wedge in the cilento area, southern Italy: a record of early apennine geodynamics. J. Geodyn. 51, 25–36. https://doi.org/10.1016/j.jog.2010.06.002.
Yamamoto, N., Ishii, Y., Hirata, R., Tetsuka, S., Yamada, T., 2023. Monitored transition from sagging to sliding during deep-seated gravitational slope deformation. Landslides, Akatani-nishi, Japan. https://doi.org/10.1007/s10346-023-02107-6.
Zhang, L., Li, J., Li, X., Zhang, J., Zhu, H., 2018. Rainfall-Induced Soil Slope Failure: Stability Analysis and Probabilistic Assessment, 1st ed. CRC Press. https://doi.org/10.1201/b20116.